Displacement-based multi-modal formulation of Koiter's method applied to cylindrical shells

Castro, Saullo G.P.; Jansen, E. L.

DOI
10.2514/6.2022-0256

Publication date
2022

Document Version
Final published version

Published in
AIAA SCITECH 2022 Forum

AIAA SciTech Forum
January 3-7, 2022, San Diego, CA & Virtual
AIAA SCITECH 2022 Forum

10.2514/6.2022-0256

Displacement-based multi-modal formulation of Koiter's method applied to cylindrical shells

S. G. P. Castro*
Faculty of Aerospace Engineering, Delft University of Technology, 2629 HS Delft, Netherlands

E. L. Jansen†
Rotterdam University of Applied Sciences, G.J. de Jonghweg 4-6, 3015 GG Rotterdam

The multi-modal formulation of Koiter's asymptotic method provides a systematic and efficient procedure to evaluate the initial post-buckling behaviour and to assess the nonlinear behavior of structures. This manuscript presents a displacement-based multi-modal formulation of Koiter's method for cylindrical shells, which are structures known for their high imperfection sensitivity and for having clustered bifurcation modes that highly interact. A third-order interpolation is used for the in-plane and out-of-plane displacements by means of the Bogner-Fox-Schmit-Castro (BFSC) element, with 4 nodes and 10 degrees-of-freedom per node, aiming at an accurate representation of the second-order fields required in the initial post-buckling analysis. The single-curvature of the shell is considered in the finite element kinematics and the study includes nonlinear kinematics from Von Kármán and Sanders. The mesh is obtained by closing the circumferentially oriented coordinate at the position where the mesh completes one revolution about the shell perimeter. The proposed formulation and implementation is verified in detail by comparing results for composite shells against established literature for multi-mode asymptotic expansions. A fast convergence of the proposed formulation is observed for linear buckling, pre-buckling state and the initial post-buckling coefficients. The developed formulation enables a close relationship between formulae and the implemented code, and is implemented using state-of-the-art collaborative software. The authors made the implemented routines in a publicly available data set with the aim to popularize Koiter's method.

I. Introduction

The asymptotic theory originally proposed by Koiter [1] has been used within semi-analytical contexts [2, 3] and has also been applied within finite element frameworks [4–13]. In recent years, the method has been applied in the analysis of imperfection sensitive shells [14–17]. Particularly the multi-modal formulation of Koiter's approach provides a systematic and efficient procedure to assess the nonlinear behavior of the structure in cases where several buckling modes interact, such as in structures highly optimized for buckling and imperfection-sensitive shell structures, where small imperfections due to variations in manufacturing parameters can induce different bifurcation paths [18, 19], which can be studied by Koiter's perturbation analysis.

The aim of the present work is to extend the multi-modal displacement-based formulation of Castro and Jansen [13] to cylindrical shells. The adopted formulation and notation keep a close correspondence between the theory and the implemented algorithms, being helpful in addressing issues experienced in the past with implementations of Koiter's asymptotic method, as highlighted by Casciaro [9].

General-purpose functional derivatives are presented and expressions for these functional derivatives are later obtained using von Kármán and Sanders nonlinear shell kinematics.

The developed formulation and implementation is verified against existing literature for multi-modal asymptotic expansion of a composite cylinder. A data set containing the implemented algorithms is made publicly available.

*Corresponding author, Assistant Professor in the Department of Aerospace Structures and Materials, email: S.G.P.Castro@tudelft.nl
†Lecturer in the School of Engineering and Applied Science, email: e.l.jansen@hr.nl

II. Multi-modal asymptotic expansion

Given a total potential energy functional $\phi[\boldsymbol{u}, \lambda]$ that depends on displacements $\boldsymbol{u}$ and a scalar load multiplier λ, a pre-buckling static equilibrium with solution $\boldsymbol{u_0}$ that corresponds to a load level λ_0 can be described as:

$$\delta\phi[\boldsymbol{u_0}, \lambda_0] = \phi'[\boldsymbol{u_0}, \lambda_0]\delta\boldsymbol{u} = 0 \tag{1}$$

Note that Eq. 1 is applicable to either a linear or a nonlinear pre-buckling state, and that the notation $\phi'\delta\boldsymbol{u}$ is used instead of $\delta\phi$ to conveniently express the functional variation as a tensor product between the Fréchet derivative ϕ' and the variation of the vector containing all degrees-of-freedom $\delta\boldsymbol{u}$ [20]. Assume that there exists at least one point of equilibrium that intersects $[\boldsymbol{u}(\lambda), \lambda]$ at a bifurcation point $[\boldsymbol{u_c}, \lambda_c]$, such that $\boldsymbol{u_c} = \lambda_c \boldsymbol{u_0}$. Here, λ_c represents the critical buckling load or critical bifurcation load. Koiter [1] proposed to express $\boldsymbol{u} - \boldsymbol{u_c}$ and $\lambda - \lambda_c$ using asymptotic expansions, representing the difference between the current displacements and the displacements at the bifurcation point, with the corresponding load increment:

$$\begin{aligned} \boldsymbol{u} - \boldsymbol{u_c} = \boldsymbol{v} &= \xi \boldsymbol{u_I} + \xi^2 \boldsymbol{u_{II}} + \xi^3 \boldsymbol{u_{III}} + \cdots \\ \lambda - \lambda_c &= a_I \lambda_c \xi + b_I \lambda_c \xi^2 + \cdots \end{aligned} \tag{2}$$

where: **(1)** ξ is a scalar parameter. **(2)** $\boldsymbol{u_I}$ is a first-order field, taken directly from one or a linear combination of multiple linear buckling modes. Vector $\boldsymbol{u_I}$ is customarily re-scaled dividing by the maximum normal displacement amplitude and multiplying by the plate or shell thickness. **(3)** $\boldsymbol{u_{II}}$ is a second-order field that provides a correction to the first-order field. **(4)** The third-order field $\boldsymbol{u_{III}}$, and higher, are assumed to have a negligible contribution. **(5)** a_I and b_I are respectively first- and second-order load parameters to be determined. Equation 2 is a reduced-order model (ROM) relating the load λ and displacement $\boldsymbol{u}$ around the equilibrium point $[\boldsymbol{u_c}, \lambda_c]$.

The necessity of considering multiple modes in the asymptotic expansion has been demonstrated by many authors. Madeo et al. [12] demonstrated that plates with variable stiffness and high aspect ratio required 4 modes to obtain a satisfactory approximation of the post-buckling behavior. Imperfection sensitive structures that usually show clustered buckling modes and clustered natural frequencies [21–23] have also been studied using the asymptotic expansion with multiple modes [14–17]. In such structures, small imperfections due to variations in manufacturing parameters can induce different bifurcation paths [18, 19], which can be studied by Koiter's multi-modal perturbation analysis. The single-mode asymptotic expansion of Eq. 2 can be generalized to a multi-modal asymptotic expansion, as shown in Eqs. 3 and 4 [13, 24]:

$$\boldsymbol{u} - \boldsymbol{u_c} = \boldsymbol{v} = \xi_i \boldsymbol{u_i} + \xi_i \xi_j \boldsymbol{u_{ij}} + \cdots \tag{3}$$

$$\xi_I(\lambda - \lambda_I) = \lambda_I a_{I\,jk} \xi_j \xi_k + \lambda_I b_{I\,jk\ell} \xi_j \xi_k \xi_\ell + \cdots \tag{4}$$

where summation convention is applied for repeated indices $j, k, \ell = 1, 2, \cdots m$ is applied. Equation 4 is a reduced-order model consisting of a system of m equations obtained for $I = 1, 2, \cdots, m$, which has $\xi_1, \xi_2, \cdots, \xi_m$ unknowns. The value λ_I correspond to the I^{th} linear buckling eigenvalue $\boldsymbol{u_I}$, always re-scaled by dividing with the maximum out-of-plane displacement and multiplying by the plate thickness. Finding the right number of linear buckling modes m in the multi-modal analysis is an essential question [9], and a proposed criterion is to select a number of modes that lies within 10%-20% departing from the first critical load [9]. In the present study, this rule proposed by Casciaro et al. will be investigated and discussed in the final manuscript, given that this is still an opened question without a generally accepted criterion.

Note that Eq. 3 consists on a reduced-order model to calculate displacements $\boldsymbol{u}$ based on a pre-buckled state $\boldsymbol{u_c}$ with known linear buckling modes $\boldsymbol{u_i}$ and known second-order displacement fields $\boldsymbol{u_{ij}}$. As in the case of the single-mode expansion, for plates and shells it is customary to re-scale $\boldsymbol{u_{ij}}$ dividing by the maximum normal displacement amplitude of $\boldsymbol{u_{ij}}$ and multiplying by the plate or shell thickness. The coefficients ξ_i for $i = 1, \ldots, m$ are found for each load λ after solving the system of m equations given by Eq. 4. Solving Eq. 4 requires the calculation of all coefficients a_{ijk} and $b_{ijk\ell}$.

The expressions given by Eqs. 3 and 4 can be applied to the expanded total potential energy functional of Eq. 5, adopting the notation of Castro and Jansen [13].

$$\begin{aligned}\phi'[\boldsymbol{u},\lambda]\delta\boldsymbol{u} = &\left(\phi_c'' + \dot{\phi}_c''(\lambda-\lambda_c) + \frac{1}{2}\ddot{\phi}_c''(\lambda-\lambda_c)^2 + \cdots\right)\boldsymbol{v}\delta\boldsymbol{u} \\ &+ \frac{1}{2}\left(\phi_c''' + \dot{\phi}_c'''(\lambda-\lambda_c) + \frac{1}{2}\ddot{\phi}_c'''(\lambda-\lambda_c)^2 + \cdots\right)\boldsymbol{v}^2\delta\boldsymbol{u} \\ &+ \frac{1}{6}\left(\phi_c^{iv} + \dot{\phi}_c^{iv}(\lambda-\lambda_c) + \frac{1}{2}\ddot{\phi}_c^{iv}(\lambda-\lambda_c)^2 + \cdots\right)\boldsymbol{v}^3\delta\boldsymbol{u} \\ &+ \cdots\end{aligned} \tag{5}$$

The resulting formula is shown in Eq. 6, where the terms multiplying $\xi_j\xi_k$ and $\xi_j\xi_k\xi_\ell$ are collected. The collected terms for the multi-modal expansion are shown in Eq. 6, where the following orthogonality property of the linear buckling modes is used: $\langle \boldsymbol{u_i}, \boldsymbol{u_j}\rangle = 0, \forall\, i \neq j$; leading to $\phi_c''\boldsymbol{u_i u_j} = 0, \forall\, i \neq j$; $\dot{\phi}_c''\boldsymbol{u_i u_j} = 0, \forall\, i \neq j$; and $\ddot{\phi}_c''\boldsymbol{u_i u_j} = 0, \forall\, i \neq j$. Moreover, collected terms in brackets that are multiplying any of the perturbation parameters $\xi_{j,k,\ell}$ ultimately vanish, knowing that $\xi_{j,k,\ell} \to 0$.

$$\begin{aligned}&\xi_j\xi_k\left[\left(a_{ijk}+a_{ikj}\right)\lambda_i\boldsymbol{u_i}\dot{\phi}_c'' + \phi_c'''\boldsymbol{u_j u_k} + \phi_c''\boldsymbol{u_{jk}} + \phi_c''\boldsymbol{u_{kj}}\right]\delta\boldsymbol{u} \\ &\quad+\xi_j\xi_k\xi_\ell\left[\lambda_i\dot{\phi}_c''\boldsymbol{u_i}\left(b_{ijk\ell}+b_{ik\ell j}+b_{i\ell kj}\right.\right. \\ &\quad\left.+b_{ij\ell k}+b_{ikj\ell}+b_{i\ell jk}\right) + \phi_c^{iv}\boldsymbol{u_j u_k u_\ell} \\ &\quad+\phi_c'''\left(\boldsymbol{u_j u_{k\ell}}+\boldsymbol{u_j u_{\ell k}}+\boldsymbol{u_k u_{j\ell}}\right. \\ &\quad\left.+\boldsymbol{u_k u_{\ell j}}+\boldsymbol{u_\ell u_{jk}}+\boldsymbol{u_\ell u_{kj}}\right) \\ &\quad+\ddot{\phi}_c''\lambda_i^2\boldsymbol{u_i}\left(a_{iij}a_{ik\ell}+a_{iji}a_{ik\ell}+a_{iij}a_{i\ell k}+a_{iji}a_{i\ell k}\right. \\ &\quad+a_{iik}a_{ij\ell}+a_{iki}a_{ij\ell}+a_{iik}a_{i\ell j}+a_{iki}a_{i\ell j} \\ &\quad\left.+a_{ii\ell}a_{ijk}+a_{i\ell i}a_{ijk}+a_{ii\ell}a_{ikj}+a_{i\ell i}a_{ikj}\right) \\ &\quad+\dot{\phi}_c'''\lambda_i\left(a_{iij}\boldsymbol{u_k u_\ell}+a_{iji}\boldsymbol{u_k u_\ell}+a_{iik}\boldsymbol{u_j u_\ell}+a_{iki}\boldsymbol{u_j u_\ell}\right. \\ &\quad+a_{ii\ell}\boldsymbol{u_j u_k}+a_{i\ell i}\boldsymbol{u_j u_k}+a_{ijk}\boldsymbol{u_i u_\ell}+a_{ikj}\boldsymbol{u_i u_\ell} \\ &\quad\left.\left.+a_{ij\ell}\boldsymbol{u_i u_k}+a_{i\ell j}\boldsymbol{u_i u_k}+a_{ik\ell}\boldsymbol{u_i u_j}+a_{i\ell k}\boldsymbol{u_i u_j}\right)\right]\delta\boldsymbol{u} \\ &+\cdots = 0\end{aligned} \tag{6}$$

For the expanded equilibrium to be stationary, each term in Eq. 6 must vanish separately. Assuming $\delta\boldsymbol{u} = \boldsymbol{u_i}$ in Eq. 6, the expressions for a_{ijk} and $b_{ijk\ell}$ of Eq. 4 can be obtained, as respectively given in Eqs. 7 and 8.

$$a_{ijk} = -\frac{1}{2\lambda_i}\frac{\phi_c'''\boldsymbol{u_i u_j u_k}}{\dot{\phi}_c''\boldsymbol{u_i u_i}} \tag{7}$$

$$\begin{aligned}b_{ijk\ell} = \frac{-1}{6\lambda_i\dot{\phi}_c''\boldsymbol{u_i u_i}}&\left[\phi_c^{iv}\boldsymbol{u_i u_j u_k u_\ell} + 3\phi_c'''\boldsymbol{u_i}\left(\boldsymbol{u_j u_{k\ell}}+\boldsymbol{u_\ell u_{jk}}\right)\right. \\ &\left.+\lambda_i\dot{\phi}_c'''\boldsymbol{u_i}\left(a_{iij}\boldsymbol{u_k u_\ell}+a_{ijk}\boldsymbol{u_\ell u_i}+a_{ik\ell}\boldsymbol{u_i u_j}\right) + \lambda_i^2\ddot{\phi}_c''\boldsymbol{u_i u_i}\left(a_{iij}a_{ik\ell}+a_{ijk}a_{i\ell i}++a_{ik\ell}a_{iij}\right)\right]\end{aligned} \tag{8}$$

Note that, in the calculation of $b_{ijk\ell}$, the second-order fields $\boldsymbol{u_{ij}}$ are needed. First, a non-orthogonal second-order field $\bar{\boldsymbol{u}}_{\boldsymbol{ij}}$ is calculated. Note that the terms in brackets multiplying $\xi_j\xi_k$ in Eq. 6 are obtained for any i^{th} mode. Therefore,

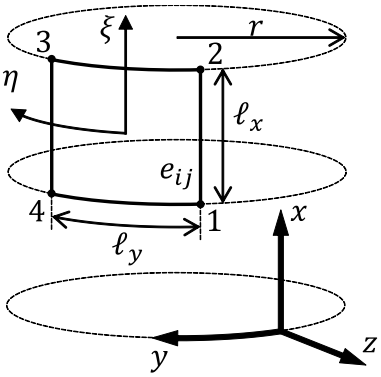

Fig. 1 Single-curvature BFSC element and the global coordinate system xyz.

the contribution for all $i = 1, \ldots, m$ modes are added and the following equation for $\bar{\boldsymbol{u}}_{\boldsymbol{ij}}$ is obtained:

$$\bar{\boldsymbol{u}}_{\boldsymbol{jk}} = \left[\phi_c''\right]^{-1} \left(-\frac{1}{2}\phi_c'''\boldsymbol{u_j u_k} - \frac{1}{m}\sum_{i=1}^{i=m} a_{ijk}\lambda_i \boldsymbol{u_i}\dot{\phi}_c'' \right) \tag{9}$$

The orthogonal second-order field vectors in the multi-modal asymptotic expansion can be obtained after successive Gram-Schmidt orthogonalization [25] operations, used to remove the components of $\bar{\boldsymbol{u}}_{\boldsymbol{jk}}$ that are parallel to all linear buckling modes used in the multi-modal expansion $\boldsymbol{u_i}$, with $i = 1, 2, \ldots, m$. This orthogonalization procedure is formulated in Eq. 10.

$$\boldsymbol{u_{jk}} = \bar{\boldsymbol{u}}_{\boldsymbol{jk}} - \sum_{i=1}^{i=m} \boldsymbol{u_i} \frac{\langle \bar{\boldsymbol{u}}_{\boldsymbol{jk}}, \boldsymbol{u_i} \rangle}{\langle \boldsymbol{u_i}, \boldsymbol{u_i} \rangle} \tag{10}$$

III. Linear buckling formulation

The objective of the present formulation is to calculate the first-order buckling states $\boldsymbol{u_i}$ used in Eqs. 7 and 8. The Bogner-Fox-Schmit-Castro (BFSC) finite element [13, 26] is a C1 contiguous confirming plate element obtained by taking tensor products of cubic Hermite splines. With 4 nodes per element and 10 degrees-of-freedom per node, the BFSC approximates the in-plane and out-of-plane displacements using 3^{rd}–order polynomials. The single-curvature BFSC element (SC–BFSC) applied by Wang et al. [27] is proposed to combine the high-order interpolation of the BFSC with cylindrical shell kinematics. Figure 1 illustrates a SC–BFSC element and a global coordinate system xyz, where coordinate y is curvilinear following the circumferential perimeter, such that at $y = 2\pi r$ the path closes on itself. The nodal connectivity is also indicated, and the mesh is built to keep the element edges parallel to the x, y coordinates, such that $\ell_x = x_2 - x_1 = x_3 - x_4$, and $\ell_y = y_4 - y_1 = y_3 - y_2$. Figure 2 shows the mesh closing on itself at the intersection of elements e_{in} with elements e_{i1}. The natural coordinates are defined as $\xi = 2x/\ell_x - 1$ and $\eta = 2y/\ell_y - 1$, and with the proposed nodal connectivity, the values of ξ_i, η_i at each node, for all elements, are:

$Node$	ξ_i	η_i
1	−1	−1
2	+1	−1
3	+1	+1
4	−1	+1

(11)

The displacements along x, y, z are respectively u, v, w and can be approximated within each element as:

$$u_e, v_e, w_e = \sum_{i=1}^{4} \boldsymbol{S}_i^{u,v,w} \boldsymbol{u_{e}}_i \tag{12}$$

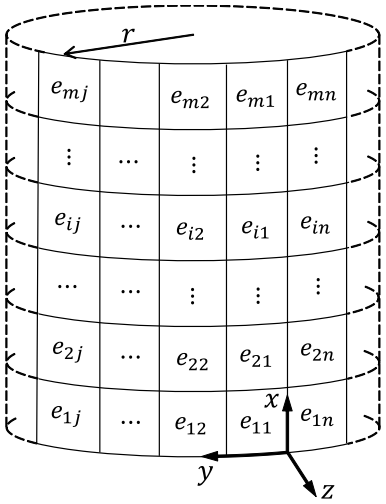

Fig. 2 SC–BFSC mesh for the cylindrical shells.

where $\boldsymbol{S}_i^{u,v,w}$ and $\boldsymbol{u_e}_i$ are the shape functions and the 10 degrees-of-freedom of the i^{th} node of the SC–BFSC element, being in the following order: u, $\partial u/\partial x$, $\partial u/\partial y$, v, $\partial v/\partial x$, $\partial v/\partial y$, w, $\partial w/\partial x$, $\partial w/\partial y$, $\partial^2 w/\partial x \partial y$. For the SC–BFSC element, the same shape functions of the plate BFSC element [13] can be used:

$$\begin{aligned}
\boldsymbol{S}_i^u &= \begin{bmatrix} H_i & H_i^x & H_i^y & 0 & 0 & 0 & 0 & 0 & 0 & 0 \end{bmatrix} \\
\boldsymbol{S}_i^v &= \begin{bmatrix} 0 & 0 & 0 & H_i & H_i^x & H_i^y & 0 & 0 & 0 & 0 \end{bmatrix} \\
\boldsymbol{S}_i^w &= \begin{bmatrix} 0 & 0 & 0 & 0 & 0 & 0 & H_i & H_i^x & H_i^y & H_i^{xy} \end{bmatrix}
\end{aligned} \tag{13}$$

with the cubic Hermite functions $H_i, H_i^x, H_i^y, H_i^{xy}$ calculated using natural coordinates [28–30]:

$$\begin{aligned}
H_i &= \tfrac{1}{16}(\xi+\xi_i)^2(\xi\xi_i-2)(\eta+\eta_i)^2(\eta\eta_i-2) \\
H_i^x &= -\tfrac{\ell_x}{32}\xi_i(\xi+\xi_i)^2(\xi\xi_i-1)(\eta+\eta_i)^2(\eta\eta_i-2) \\
H_i^y &= -\tfrac{\ell_y}{32}(\xi+\xi_i)^2(\xi\xi_i-2)\eta_i(\eta+\eta_i)^2(\eta\eta_i-1) \\
H_i^{xy} &= \tfrac{\ell_x\ell_y}{64}\xi_i(\xi+\xi_i)^2(\xi\xi_i-1)\eta_i(\eta+\eta_i)^2(\eta\eta_i-1)
\end{aligned} \tag{14}$$

where ℓ_x, ℓ_y are respectively the finite element dimensions along x, y, as shown in Figure 1. Using the proposed nodal connectivity for the SC–BFSC element, the nodal degrees-of-freedom $\boldsymbol{u_e}_i$ and the respective shape functions $\boldsymbol{S}_i^{u,v,w}$ are concatenated as:

$$\begin{aligned}
\boldsymbol{u_e} &= \begin{Bmatrix} \boldsymbol{u_e}_1 & \boldsymbol{u_e}_2 & \boldsymbol{u_e}_3 & \boldsymbol{u_e}_4 \end{Bmatrix}^\top \\
\boldsymbol{S}^u &= \begin{bmatrix} \boldsymbol{S}_1^u & \boldsymbol{S}_2^u & \boldsymbol{S}_3^u & \boldsymbol{S}_4^u \end{bmatrix} \\
\boldsymbol{S}^v &= \begin{bmatrix} \boldsymbol{S}_1^v & \boldsymbol{S}_2^v & \boldsymbol{S}_3^v & \boldsymbol{S}_4^v \end{bmatrix} \\
\boldsymbol{S}^w &= \begin{bmatrix} \boldsymbol{S}_1^w & \boldsymbol{S}_2^w & \boldsymbol{S}_3^w & \boldsymbol{S}_4^w \end{bmatrix}
\end{aligned} \tag{15}$$

with $\boldsymbol{S}^u$, $\boldsymbol{S}^v$ and $\boldsymbol{S}^w$ being matrices of shape 1×40.

The total potential energy of the cylindrical shell under axial compression can be represented by Eq. 16, where Ω represents the shell domain and $\delta\Omega$ the shell boundaries, i.e. the loaded edges. The first term represents the strain

energy based on equivalent single-layer theories [31, 32], whereas the second term represents the work done by external forces at the boundaries $\widehat{\boldsymbol{N}}$ multiplied by a scalar λ, with $\widehat{\boldsymbol{N}}$ expressed in force per length units.

$$\phi = \frac{1}{2}\int_{\Omega} \left(\boldsymbol{N}\boldsymbol{\varepsilon} + \boldsymbol{M}\boldsymbol{\kappa}\right) d\Omega - \int_{\delta\Omega} \lambda \widehat{\boldsymbol{N}}^{\top}\boldsymbol{u} d(\delta\Omega) \tag{16}$$

The strain energy functional of the entire shell continuum is built from the individual contributions of all finite elements ϕ_e:

$$\phi_e = \frac{1}{2}\int_{y=y_1}^{y_4}\int_{x=x_1}^{x_2} \left(\boldsymbol{N}\boldsymbol{\varepsilon} + \boldsymbol{M}\boldsymbol{\kappa}\right) dxdy \tag{17}$$

where the membrane forces are $\boldsymbol{N} = \left\{N_{xx}, N_{yy}, N_{xy}\right\}^{\top}$ and the distributed moments are $\boldsymbol{M} = \left\{M_{xx}, M_{yy}, M_{xy}\right\}^{\top}$. The integration limits $x_1 \leq x \leq x_2$ and $y_1 \leq y \leq y_4$ define the domain of one finite element Ω_e. The membrane $\boldsymbol{\varepsilon}$ and rotational $\boldsymbol{\kappa}$ strains are assumed to follow von Kármán kinematics, also referred to in the literature as Donnell-type [33, 34] or Kirchhoff-Love non-linear equations, given by:

$$\begin{aligned}
\boldsymbol{\varepsilon} &= \begin{Bmatrix} \varepsilon_{xx} \\ \varepsilon_{yy} \\ \gamma_{xy} \end{Bmatrix} = \begin{Bmatrix} u_{,x} + \frac{1}{2}w_{,x}^2 \\ v_{,y} + \frac{1}{r}w + \frac{1}{2}w_{,y}^2 \\ u_{,y} + v_{,x} + w_{,x}w_{,y} \end{Bmatrix} \\
\boldsymbol{\kappa} &= \begin{Bmatrix} \kappa_{xx} \\ \kappa_{yy} \\ \kappa_{xy} \end{Bmatrix} = \begin{Bmatrix} -w_{,xx} \\ -w_{,yy} \\ -2w_{,xy} \end{Bmatrix}
\end{aligned} \tag{18}$$

with $(\cdot)_{,x} = \partial(\cdot)/\partial x$ used as a compact notation for partial derivatives.

For Sanders-type kinematics [35], also discussed in references [36, 37] for cylindrical shells, and in references [38–41] for conical shells:

$$\begin{aligned}
\boldsymbol{\varepsilon} &= \begin{Bmatrix} \varepsilon_{xx} \\ \varepsilon_{yy} \\ \gamma_{xy} \end{Bmatrix} = \begin{Bmatrix} u_{,x} + \frac{1}{2}w_{,x}^2 \\ v_{,y} + \frac{1}{r}w + \frac{1}{2}w_{,y}^2 + \frac{1}{2}\frac{1}{r^2}v^2 - \frac{1}{r}vw_{,y} \\ u_{,y} + v_{,x} + w_{,x}w_{,y} - \frac{1}{r}vw_{,x} \end{Bmatrix} \\
\boldsymbol{\kappa} &= \begin{Bmatrix} \kappa_{xx} \\ \kappa_{yy} \\ \kappa_{xy} \end{Bmatrix} = \begin{Bmatrix} -w_{,xx} \\ -w_{,yy} + \frac{1}{r}v_{,y} \\ -2w_{,xy} + \frac{1}{r}v_{,x} \end{Bmatrix}
\end{aligned} \tag{19}$$

Unless otherwise specified, all the following derivations will assume Donnell-type kinematics. At the bifurcation point, the following state of equilibrium exists, considering all n_e elements:

$$\delta\phi = \sum_{e=1}^{n_e} \delta\phi_e - \int_{\delta\Omega} \lambda \widehat{\boldsymbol{N}}^{\top}\delta\boldsymbol{u} d(\delta\Omega) = \left[\sum_{e=1}^{n_e}\int_{\Omega_e} \left(\boldsymbol{N}^{\top}\delta\boldsymbol{\varepsilon} + \boldsymbol{M}^{\top}\delta\boldsymbol{\kappa}\right) d\Omega_e\right] - \int_{\delta\Omega} \lambda \widehat{\boldsymbol{N}}^{\top}\delta\boldsymbol{u} d(\delta\Omega) = 0 \tag{20}$$

Expressing the displacements within one element in terms of nodal coordinates $\boldsymbol{u_e}$ as per Eq. 12, $\delta\boldsymbol{\varepsilon}$ and $\delta\boldsymbol{\kappa}$ can be calculated from Eq. 18 as:

$$\delta\boldsymbol{\varepsilon} = \begin{bmatrix} \boldsymbol{S}^u_{,x} + w_{,x}\boldsymbol{S}^w_{,x} \\ \boldsymbol{S}^v_{,y} + \frac{1}{r}\boldsymbol{S}^w + w_{,y}\boldsymbol{S}^w_{,y} \\ \boldsymbol{S}^u_{,y} + \boldsymbol{S}^v_{,x} + w_{,x}\boldsymbol{S}^w_{,y} + w_{,y}\boldsymbol{S}^w_{,x} \end{bmatrix} \delta\boldsymbol{u_e}$$
$$\delta\boldsymbol{\kappa} = \begin{bmatrix} -\boldsymbol{S}^w_{,xx} \\ -\boldsymbol{S}^w_{,yy} \\ -2\boldsymbol{S}^w_{,xy} \end{bmatrix} \delta\boldsymbol{u_e} \tag{21}$$

where the partial derivatives of $\boldsymbol{S}^{u,v,w}$ are directly calculated from the shape functions of Eq. 13 in terms of the natural coordinates ξ, η, using the following Jacobian relations:

$$\frac{\partial}{\partial x} = \frac{\ell_x}{2}\frac{\partial}{\partial \xi}$$
$$\frac{\partial}{\partial y} = \frac{\ell_y}{2}\frac{\partial}{\partial \eta} \tag{22}$$

The neutral equilibrium criterion also requires that $\delta^2\phi_e = 0$ [41], such that, from Eq. 20:

$$\delta^2\phi = \sum_{e=1}^{n_e} \delta^2\phi_e = \sum_{e=1}^{n_e} \left[\int_{\Omega_e} \left(\delta\boldsymbol{N}^\top \delta\boldsymbol{\varepsilon} + \delta\boldsymbol{M}^\top \delta\boldsymbol{\kappa} \right) d\Omega_e + \int_{\Omega_e} \left(\boldsymbol{N}^\top \delta^2\boldsymbol{\varepsilon} + \boldsymbol{M}^\top \delta^2\boldsymbol{\kappa} \right) d\Omega_e \right] = 0 \tag{23}$$

The first integral of Eq. 23 becomes the constitutive stiffness matrix of the element, calculated using the constitutive relations from classical laminated plate theory [32]:

$$\delta\boldsymbol{N} = \boldsymbol{A}\delta\boldsymbol{\varepsilon} + \boldsymbol{B}\delta\boldsymbol{\kappa}$$
$$\delta\boldsymbol{M} = \boldsymbol{B}\delta\boldsymbol{\varepsilon} + \boldsymbol{D}\delta\boldsymbol{\kappa}$$

Note that the geometric non-linearity appears in the constitutive stiffness matrix due to $w_{,x}, w_{,y}$ in Eq. 21. Therefore, the linear constitutive stiffness matrix of a finite element $\boldsymbol{K_e}$ is calculated by assuming $w_{,x}, w_{,y} = 0$, leading to a 40×40 matrix:

$$\begin{aligned} \boldsymbol{K_e} = \iint_{xy} \Bigg(& \begin{bmatrix} \boldsymbol{S}^u_{,x} \\ \boldsymbol{S}^v_{,y} + \frac{1}{r}\boldsymbol{S}^w \\ \boldsymbol{S}^u_{,y} + \boldsymbol{S}^v_{,x} \end{bmatrix}^\top \boldsymbol{A} \begin{bmatrix} \boldsymbol{S}^u_{,x} \\ \boldsymbol{S}^v_{,y} + \frac{1}{r}\boldsymbol{S}^w \\ \boldsymbol{S}^u_{,y} + \boldsymbol{S}^v_{,x} \end{bmatrix} \\ & + \begin{bmatrix} \boldsymbol{S}^u_{,x} \\ \boldsymbol{S}^v_{,y} + \frac{1}{r}\boldsymbol{S}^w \\ \boldsymbol{S}^u_{,y} + \boldsymbol{S}^v_{,x} \end{bmatrix}^\top \boldsymbol{B} \begin{bmatrix} -\boldsymbol{S}^w_{,xx} \\ -\boldsymbol{S}^w_{,yy} \\ -2\boldsymbol{S}^w_{,xy} \end{bmatrix} + \begin{bmatrix} -\boldsymbol{S}^w_{,xx} \\ -\boldsymbol{S}^w_{,yy} \\ -2\boldsymbol{S}^w_{,xy} \end{bmatrix}^\top \boldsymbol{B} \begin{bmatrix} \boldsymbol{S}^u_{,x} \\ \boldsymbol{S}^v_{,y} + \frac{1}{r}\boldsymbol{S}^w \\ \boldsymbol{S}^u_{,y} + \boldsymbol{S}^v_{,x} \end{bmatrix} \\ & + \begin{bmatrix} -\boldsymbol{S}^w_{,xx} \\ -\boldsymbol{S}^w_{,yy} \\ -2\boldsymbol{S}^w_{,xy} \end{bmatrix}^\top \boldsymbol{D} \begin{bmatrix} -\boldsymbol{S}^w_{,xx} \\ -\boldsymbol{S}^w_{,yy} \\ -2\boldsymbol{S}^w_{,xy} \end{bmatrix} \Bigg) dxdy \end{aligned} \tag{24}$$

The second integral of Eq. 23 becomes the geometric stiffness matrix of the finite element $\boldsymbol{K_{G0e}}$, capturing the geometrically nonlinear effects of a linear pre-buckling membrane stresses $\boldsymbol{N_0} = \left\{N_{0xx}, N_{0yy}, N_{0xy}\right\}^\top$ on the membrane stiffness. Noting that $\delta^2\boldsymbol{\kappa} = \boldsymbol{0}$ [13, 41], the equation for $\boldsymbol{K_{G0e}}$ becomes:

$$\boldsymbol{K_{G0e}} = \iint_{xy} \begin{bmatrix} \boldsymbol{S}_{,x}^{w\top} N_{0xx} \boldsymbol{S}_{,x}^{w} \\ \boldsymbol{S}_{,y}^{w\top} N_{0yy} \boldsymbol{S}_{,y}^{w} \\ \boldsymbol{S}_{,y}^{w\top} N_{0xy} \boldsymbol{S}_{,x}^{w} + \boldsymbol{S}_{,x}^{w\top} N_{0xy} \boldsymbol{S}_{,y}^{w} \end{bmatrix} dxdy \tag{25}$$

The contributions all n_e finite element are added to build the global constitutive stiffness matrix $\boldsymbol{K}$ and geometric stiffness matrix $\boldsymbol{K_{G0}}$ of the system:

$$\begin{aligned} \boldsymbol{K} &= \sum_{e=1}^{n_e} \boldsymbol{K_e} \\ \boldsymbol{K_{G0}} &= \sum_{e=1}^{n_e} \boldsymbol{K_{G0e}} \end{aligned} \tag{26}$$

The linear pre-buckling stress field of one finite element $N_{0xx}, N_{0yy}, N_{0xy}$ is calculated from the corresponding nodal displacements $\boldsymbol{u_{0e}}$ as:

$$\boldsymbol{N_0} = \begin{Bmatrix} N_{0xx} \\ N_{0yy} \\ N_{0xy} \end{Bmatrix} = \boldsymbol{A} \begin{bmatrix} \boldsymbol{S}_{,x}^{u} \\ \boldsymbol{S}_{,y}^{v} + \frac{1}{r}\boldsymbol{S}^{w} \\ \boldsymbol{S}_{,y}^{u} + \boldsymbol{S}_{,x}^{v} \end{bmatrix} \boldsymbol{u_{0e}} \tag{27}$$

where $\boldsymbol{u_{0e}}$ is directly extracted from the full pre-buckling displacement vector $\boldsymbol{u_0}$ that can be obtained from a linear static analysis, derived from the equilibrium of Eq. 20:

$$\boldsymbol{u_0} = \boldsymbol{K}^{-1}\boldsymbol{f_0} \tag{28}$$

with $\boldsymbol{f_0}$ represents any general pre-buckling force. When applying the neutral equilibrium criterion of Eq. 23 one assumes that at the bifurcation point there is a value of internal membrane stresses $\boldsymbol{N}$ based on the known linear pre-buckling stress $\boldsymbol{N_0}$ described by $\boldsymbol{N} = \lambda\boldsymbol{N_0}$, which leads to the condition $\delta^2\phi = 0$. Therefore, the problem consists of finding the value of λ that leads to:

$$\delta\boldsymbol{u}^\top \left(\boldsymbol{K} + \lambda\boldsymbol{K_{G0}}\right) \delta\boldsymbol{u} = 0 \tag{29}$$

which holds true for any variation $\delta\boldsymbol{u}$, such that the required condition for the equality of Eq. 29 is:

$$\det\left(\boldsymbol{K} + \lambda\boldsymbol{K_{G0}}\right) = 0 \tag{30}$$

Equation 30 represents a linear buckling eigenvalue problem, where a characteristic polynomial in terms of λ can be obtained and solved. For a system with n unknown degrees-of-freedom, there are n eigenvalues that are roots of the characteristic polynomial. In practice, the eigenvalues and corresponding buckling modes are solved using generalized eigenvalue solvers that are able to efficiently extract only a desired number of eigenvalues and buckling modes, and in the present work the locally optimal block preconditioned conjugate gradient method [42] implemented in SciPy [43] is used. We refer to the lowest eigenvalue as being the critical linear buckling load λ_c.

The integration of $\boldsymbol{K_e}$ and $\boldsymbol{K_{G0e}}$ over the finite element domains are performed numerically using standard Gauss-quadrature with 4×4 integration points per element. The authors verified that this amount of integration points

leads to a converged behavior even for variable-stiffness filament-wound cylinders [27]. For each integration point, the local shell constitutive properties are calculated, with the elements of the constitutive matrices given by A_{ij}, B_{ij}, D_{ij}:

$$\begin{aligned} A_{ij} &= \sum_{k=1}^{n} Q_{ij}\,(z_k - z_{k-1}) \\ B_{ij} &= \sum_{k=1}^{n} Q_{ij}\,\tfrac{1}{2}\left(z_k^2 - z_{k-1}^2\right) \\ D_{ij} &= \sum_{k=1}^{n} Q_{ij}\,\tfrac{1}{3}\left(z_k^3 - z_{k-1}^3\right) \end{aligned} \tag{31}$$

where n is the number of plies; Q_{ij} is the ply stiffness expressed in laminate coordinates [32]; z_k and z_{k-1} define respectively the positions of the outward and inward face of the k^{th} ply, according to the coordinate system of Figure 1.

IV. Higher-order derivatives

A. Strains using Von Kármán kinematics

The functional derivatives leading to the n^{th}–order tensors $\phi_c^{(n)}$, $\dot{\phi}_c^{(n)}$ and $\ddot{\phi}_c^{(n)}$ were obtained during the multi-modal asymptotic expansions. Assuming the kinematic relations of Eq. 18, and the approximation for the displacements given by Eq. 12, the strain variations can be represented as:

$$\begin{aligned} \delta\boldsymbol{\varepsilon} &= \boldsymbol{\varepsilon}'\delta\boldsymbol{u} \\ \delta\boldsymbol{\kappa} &= \boldsymbol{\kappa}'\delta\boldsymbol{u} \end{aligned} \tag{32}$$

where the $'$ (prime) symbol is used to denote a Fréchet's differentiation. Ordering the strain components as $\varepsilon_1 = \varepsilon_{xx}, \varepsilon_2 = \varepsilon_{yy}, \varepsilon_3 = \gamma_{xy}, \kappa_1 = \kappa_{xx}, \kappa_2 = \kappa_{yy}, \kappa_3 = \kappa_{xy}$; and adopting summation convention for repeated indices, with $a = 1, 2, \cdots, n$; the first and second variations of the extensional and rotational strains become:

$$\begin{aligned} \delta\varepsilon_i &= \varepsilon'_{ia}\delta u_a \\ \delta\kappa_i &= \kappa'_{ia}\delta u_a \\ \delta(\delta\varepsilon_i) &= \varepsilon''_{iab}\delta u_a\delta u_b \\ \delta(\delta\kappa_i) &= \kappa''_{iab}\delta u_a\delta u_b \end{aligned} \tag{33}$$

With these definitions, the first variation of the strains given by Eq. 21 can be represented by means of first Fréchet's differentiation as:

$$\boldsymbol{\varepsilon}'_a = \begin{Bmatrix} S^u_{a,x} + w_{,x}S^w_{a,x} \\ S^v_{a,y} + \frac{1}{r}S^w_a + w_{,y}S^w_{a,y} \\ S^u_{a,y} + S^v_{a,x} + w_{,x}S^w_{a,y} + w_{,y}S^w_{a,x} \end{Bmatrix}$$

$$\boldsymbol{\kappa}'_a = \begin{Bmatrix} -S^w_{a,xx} \\ -S^w_{a,yy} \\ -2S^w_{a,xy} \end{Bmatrix} \tag{34}$$

For a linear pre-buckling state, or linear fundamental state, the nonlinear terms of Eq. 34 are ignored. For a nonlinear pre-buckling, or nonlinear fundamental state, the values or $w_{,x}$ and $w_{,y}$ are calculated based on the nonlinear pre-buckling state at the load level λ_c [44].

The second Fréchet's differentiation of the strains leads to:

$$\boldsymbol{\varepsilon}''_{ab} = \begin{Bmatrix} S^w_{a,x} S^w_{b,x} \\ S^w_{a,y} S^w_{b,y} \\ S^w_{a,y} S^w_{b,x} + S^w_{a,x} S^w_{b,y} \end{Bmatrix} \qquad \boldsymbol{\kappa}''_{ab} = \mathbf{0} \tag{35}$$

Note in Eq. 35 that ε''_{iab} represents a symmetric second-order tensor, which is an important property to be considered while implementing the method.

For the differentiations with respect to λ, we must recall that all functional expansions were calculated about the bifurcation point $[\boldsymbol{u_c}, \lambda_c]$, such that the strains and stresses are those corresponding to the displacement $\boldsymbol{u_c} = \lambda \boldsymbol{u_0}$, with $\lambda = \lambda_c$. Starting with $\boldsymbol{\varepsilon}$ and $\boldsymbol{\kappa}$, using the notation $\partial(\cdot)/\partial\lambda = \dot{(\cdot)}$ and $\partial^2(\cdot)/\partial\lambda^2 = \ddot{(\cdot)}$:

$$\dot{\boldsymbol{\varepsilon}} = \begin{Bmatrix} u_{0,x} + \lambda w_{0,x}^2 \\ v_{0,y} + \frac{1}{r} w_0 + \lambda w_{0,y}^2 \\ u_{0,y} + v_{0,x} + 2\lambda w_{0,x} w_{0,y} \end{Bmatrix} \qquad \dot{\boldsymbol{\kappa}} = \begin{Bmatrix} -w_{0,xx} \\ -w_{0,yy} \\ -2w_{0,xy} \end{Bmatrix} \tag{36}$$

For a linear pre-buckling state, $\boldsymbol{u_0}$ is evaluated as per Eq. 28 and the nonlinear terms in Eq. 36 can be ignored, such that the initial post-buckling analysis is greatly simplified. Nevertheless, the formulation presented next is valid for the more general case of a nonlinear pre-buckling state. The second differentiation with respect to λ gives:

$$\ddot{\boldsymbol{\varepsilon}} = \begin{Bmatrix} w_{0,x}^2 \\ w_{0,y}^2 \\ 2w_{0,x} w_{0,y} \end{Bmatrix} \qquad \ddot{\boldsymbol{\kappa}} = \mathbf{0} \tag{37}$$

For $\boldsymbol{\varepsilon}'_a$ and $\boldsymbol{\kappa}'_a$, the first differentiation with respect to λ gives:

$$\dot{\boldsymbol{\varepsilon}}'_a = \begin{Bmatrix} w_{0,x} S^w_{a,x} \\ w_{0,y} S^w_{a,y} \\ w_{0,x} S^w_{a,y} + w_{0,y} S^w_{a,x} \end{Bmatrix} \qquad \dot{\boldsymbol{\kappa}}'_a = \mathbf{0} \tag{38}$$

For the second differentiations with respect to λ, $\ddot{\boldsymbol{\varepsilon}}'_a = \mathbf{0}$ and $\ddot{\boldsymbol{\kappa}}'_a = \mathbf{0}$. For $\boldsymbol{\varepsilon}''_{ab}$ and $\boldsymbol{\kappa}''_{ab}$ all derivatives with respect to λ are zero.

B. Strains using Sanders kinematics

Assuming the kinematic relations of Eq. 19, the first Fréchet's differentiation of the strains renders:

$$\boldsymbol{\varepsilon}'_a = \begin{Bmatrix} S^u_{a,x} + w_{,x} S^w_{a,x} \\ S^v_{a,y} + \frac{1}{r} S^w_a + w_{,y} S^w_{a,y} + \frac{1}{r^2} v S^v_a - \frac{1}{r} v S^w_{a,y} - \frac{1}{r} w_{,y} S^v_a \\ S^u_{a,y} + S^v_{a,x} + w_{,x} S^w_{a,y} + w_{,y} S^w_{a,x} - \frac{1}{r} v S^w_{a,x} - \frac{1}{r} w_{,x} S^v_a \end{Bmatrix}$$

$$\boldsymbol{\kappa}'_a = \begin{Bmatrix} -S^w_{a,xx} \\ -S^w_{a,yy} + \frac{1}{r} S^v_{a,y} \\ -2S^w_{a,xy} + \frac{1}{r} S^v_{a,x} \end{Bmatrix} \tag{39}$$

For a linear pre-buckling state, or linear fundamental state, the nonlinear terms of Eq. 39 are ignored. For a nonlinear pre-buckling, or nonlinear fundamental state, the values or $w_{,x}$, $w_{,y}$ and v are calculated based on the nonlinear pre-buckling state at the load level λ_c [44].

The second Fréchet's differentiation of the strains becomes:

$$\boldsymbol{\varepsilon}''_{ab} = \begin{Bmatrix} S^w_{a,x} S^w_{b,x} \\ S^w_{a,y} S^w_{b,y} + \frac{1}{r^2} S^v_a S^v_b - \frac{1}{r} S^w_{a,y} S^v_b - \frac{1}{r} S^v_a S^w_{b,y} \\ S^w_{a,y} S^w_{b,x} + S^w_{a,x} S^w_{b,y} - \frac{1}{r} S^w_{a,x} S^v_b - \frac{1}{r} S^v_a S^w_{b,x} \end{Bmatrix}$$

$$\boldsymbol{\kappa}''_{ab} = \mathbf{0} \tag{40}$$

Again, as for the Von Kármán strains, ε''_{iab} of in Eq. 40 represents a symmetric second-order tensor.

Differentiating with respect to λ, starting with $\boldsymbol{\varepsilon}$ and $\boldsymbol{\kappa}$:

$$\dot{\boldsymbol{\varepsilon}} = \begin{Bmatrix} u_{0,x} + \lambda w_{0,x}^2 \\ v_{0,y} + \frac{1}{r} w_0 + \lambda w_{0,y}^2 + \lambda \frac{1}{r^2} v_0^2 - 2\lambda \frac{1}{r} v_0 w_{0,y} \\ u_{0,y} + v_{0,x} + 2\lambda w_{0,x} w_{0,y} - 2\lambda \frac{1}{r} v_0 w_{0,x} \end{Bmatrix}$$

$$\dot{\boldsymbol{\kappa}} = \begin{Bmatrix} -w_{0,xx} \\ -w_{0,yy} + \frac{1}{r} v_{0,y} \\ -2w_{0,xy} + \frac{1}{r} v_{0,x} \end{Bmatrix} \tag{41}$$

The second differentiation with respect to λ gives:

$$\ddot{\boldsymbol{\varepsilon}} = \begin{Bmatrix} w_{0,x}^2 \\ w_{0,y}^2 + \frac{1}{r^2} v_0^2 - 2\frac{1}{r} v_0 w_{0,y} \\ 2w_{0,x} w_{0,y} - 2\frac{1}{r} v_0 w_{0,x} \end{Bmatrix}$$

$$\ddot{\boldsymbol{\kappa}} = \mathbf{0} \tag{42}$$

For $\boldsymbol{\varepsilon}'_a$ and $\boldsymbol{\kappa}'_a$, the first differentiation with respect to λ gives:

$$\dot{\boldsymbol{\varepsilon}}'_a = \begin{Bmatrix} w_{0,x} S^w_{a,x} \\ w_{0,y} S^w_{a,y} + \frac{1}{r^2} v_0 S^v_a - \frac{1}{r} v_0 S^w_{a,y} - \frac{1}{r} w_{0,y} S^v_a \\ w_{0,x} S^w_{a,y} + w_{0,y} S^w_{a,x} - \frac{1}{r} v_0 S^w_{a,x} - \frac{1}{r} w_{0,x} S^v_a \end{Bmatrix} \qquad \dot{\boldsymbol{\kappa}}'_a = \mathbf{0} \tag{43}$$

Similarly to the case of Von Kármán strains, for the second differentiations with respect to λ, $\ddot{\boldsymbol{\varepsilon}}'_a = \mathbf{0}$ and $\ddot{\boldsymbol{\kappa}}'_a = \mathbf{0}$. Additionally, for $\boldsymbol{\varepsilon}''_{ab}$ and $\boldsymbol{\kappa}''_{ab}$, all derivatives with respect to λ are zero.

C. Stresses

Based on Eqs. 18 - 38 it is straightforward to compute the corresponding stresses. Using classical constitutive relations for laminated composites [32] and adopting the index notation: $N_1 = N_{xx}$, $N_2 = N_{yy}$ and $N_3 = N_{xy}$; $M_1 = M_{xx}$, $M_2 = M_{yy}$ and $M_3 = M_{xy}$; the stress-strain relations can be written as:

$$\begin{aligned} N_i &= A_{ij}\varepsilon_j + B_{ij}\kappa_j \\ M_i &= B_{ij}\varepsilon_j + D_{ij}\kappa_j \end{aligned} \tag{44}$$

where A_{ij} represents the shell membrane stiffness; B_{ij} the membrane-bending coupling stiffness; and D_{ij} the bending stiffness; all for $i, j = 1, 2, 3$. The first Fréchet derivative of the stress terms are:

$$\begin{aligned} N'_{ia} &= A_{ij}\varepsilon'_{ja} + B_{ij}\kappa'_{ja} \\ M'_{ia} &= B_{ij}\varepsilon'_{ja} + D_{ij}\kappa'_{ja} \end{aligned} \tag{45}$$

Recalling from Eq. 35 that $\kappa''_{jab} = 0$, the second Fréchet derivatives are:

$$\begin{aligned} N''_{iab} &= A_{ij}\varepsilon''_{jab} \\ M''_{iab} &= B_{ij}\varepsilon''_{jab} \end{aligned} \tag{46}$$

Note that N''_{iab}, M''_{iab} are symmetric second-order tensors. The first derivatives with respect to λ can be readily computed as:

$$\begin{aligned} \dot{N}_i &= A_{ij}\dot{\varepsilon}_j + B_{ij}\dot{\kappa}_j \\ \dot{M}_i &= B_{ij}\dot{\varepsilon}_j + D_{ij}\dot{\kappa}_j \end{aligned} \tag{47}$$

$$\begin{aligned} \dot{N}'_{ia} &= A_{ij}\dot{\varepsilon}'_{ja} \\ \dot{M}'_{ia} &= B_{ij}\dot{\varepsilon}'_{ja} \end{aligned} \tag{48}$$

$$\begin{aligned} \dot{N}''_{iab} &= 0 \\ \dot{M}''_{iab} &= 0 \end{aligned} \tag{49}$$

Finally, the second derivatives about λ are:

$$\begin{aligned}
\ddot{N}_i &= A_{ij}\ddot{\varepsilon}_j \\
\ddot{M}_i &= B_{ij}\ddot{\varepsilon}_j \\
\ddot{N}'_{ia} &= 0 \\
\ddot{M}'_{ia} &= 0 \\
\ddot{N}''_{iab} &= 0 \\
\ddot{M}''_{iab} &= 0
\end{aligned} \tag{50}$$

D. Functional derivatives

Assuming a general loading vector with distributed forces $\widehat{\boldsymbol{N}}$ at the cylinder boundaries $\delta\Omega$, the total potential energy can be written as:

$$\phi = \frac{1}{2}\int_{\Omega}\left(N_i\varepsilon_i + M_i\kappa_i\right)d\Omega - \int_{\delta\Omega}\lambda\widehat{\boldsymbol{N}}^{\intercal}\boldsymbol{u}d(\delta\Omega) \tag{51}$$

where $d\Omega = dxdy$ and summation convention is adopted for terms with repeated index i with $i = 1, 2, 3$. The stationary total potential energy at $[\boldsymbol{u_c}, \lambda_c]$ is defined as $\phi'_c = \phi'[\boldsymbol{u_c}, \lambda_c]$, calculated using the first variation of $\phi_c = \phi[\boldsymbol{u_c}, \lambda_c]$:

$$\phi'_c\delta\boldsymbol{u} = \left[\frac{1}{2}\int_{\Omega}\left(\delta N_i\varepsilon_i + N_i\delta\varepsilon_i + \delta M_i\kappa_i + M_i\delta\kappa_i\right)d\Omega - \int_{\delta\Omega}\lambda\widehat{\boldsymbol{N}}^{\intercal}\delta\boldsymbol{u}d(\delta\Omega)\right] \tag{52}$$

The variation $\delta\boldsymbol{u}$ is defined as $\delta\boldsymbol{u} = \boldsymbol{u_a} = \{\cdots, u_a, \cdots\}^{\intercal}$, and the loaded boundaries are located at $x = 0$ and $x = L$; such that the first Fréchet derivative of the total potential energy becomes:

$$\phi'_c\boldsymbol{u_a} = \left[\frac{1}{2}\int_{\Omega}\left(N'_{ia}\varepsilon_i + N_i\varepsilon'_{ia} + M'_{ia}\kappa_i + M_i\kappa'_{ia}\right)d\Omega - \int_{\delta\Omega}\lambda\widehat{\boldsymbol{N}}^{\intercal}S^{\boldsymbol{u}}_{a\,x=0}d(\delta\Omega) - \int_{\delta\Omega}\lambda\widehat{\boldsymbol{N}}^{\intercal}S^{\boldsymbol{u}}_{a\,x=L}d(\delta\Omega)\right]u_a \tag{53}$$

Resuming with the second Fréchet derivative, now replacing $\delta\boldsymbol{u}$ with $\delta\boldsymbol{u} = \boldsymbol{u_b} = \{\cdots, u_b, \cdots\}^{\intercal}$:

$$\begin{aligned}
\phi''_c\boldsymbol{u_a}\boldsymbol{u_b} = \Bigg[\frac{1}{2}\int_{\Omega}\Bigg(&N''_{iab}\varepsilon_i + N'_{ia}\varepsilon'_{ib} + N'_{ib}\varepsilon'_{ia} + N_i\varepsilon''_{iab} + M''_{iab}\kappa_i + M'_{ia}\kappa'_{ib} + M'_{ib}\kappa'_{ia} + \cancelto{0}{M_i\kappa''_{iab}}\Bigg)d\Omega\Bigg]u_au_b \\
&= \left[\frac{1}{2}\int_{\Omega}\left(N''_{iab}\varepsilon_i + N'_{ia}\varepsilon'_{ib} + N'_{ib}\varepsilon'_{ia} + N_i\varepsilon''_{iab} + M''_{iab}\kappa_i + M'_{ia}\kappa'_{ib} + M'_{ib}\kappa'_{ia}\right)d\Omega\right]u_au_b
\end{aligned} \tag{54}$$

Note that ϕ''_c in Eq. 54 represents a second-order tensor with all geometrically non-linear terms present. If a linear pre-buckling state is assumed, $\phi''_c = \boldsymbol{K} + \lambda\boldsymbol{K_{G0}}$, with $\boldsymbol{K}$ and $\boldsymbol{K_{G0}}$ defined in Eq. 26. For a nonlinear pre-buckling, or nonlinear fundamental state, ϕ''_c becomes the tangent stiffness matrix of a system in the case with no follower forces. Continuing with the third Fréchet derivative, now using $\delta\boldsymbol{u} = \boldsymbol{u_c} = \{\cdots, u_c, \cdots\}^{\intercal}$:

$$\begin{aligned}
\phi'''_c\boldsymbol{u_a}\boldsymbol{u_b}\boldsymbol{u_c} = \Bigg[\frac{1}{2}\int_{\Omega}\Bigg(&\cancelto{0}{N'''_{iabc}}\varepsilon_i + N''_{iab}\varepsilon'_{ic} + N''_{iac}\varepsilon'_{ib} + N'_{ia}\varepsilon''_{ibc} + N''_{ibc}\varepsilon'_{ia} + N'_{ib}\varepsilon''_{iac} + N'_{ic}\varepsilon''_{iab} \\
&+ N_i\cancelto{0}{\varepsilon'''_{iabc}} + \cancelto{0}{M'''_{iabc}}\kappa_i + M''_{iab}\kappa'_{ic} + M''_{iac}\kappa'_{ib} + M'_{ia}\cancelto{0}{\kappa''_{ibc}} + M''_{ibc}\kappa'_{ia} + M'_{ib}\cancelto{0}{\kappa''_{iac}}\Bigg)d\Omega\Bigg]u_au_bu_c \\
= \Bigg[\frac{1}{2}\int_{\Omega}\Bigg(&N''_{iab}\varepsilon'_{ic} + N''_{iac}\varepsilon'_{ib} + N'_{ia}\varepsilon''_{ibc} + N''_{ibc}\varepsilon'_{ia} + N'_{ib}\varepsilon''_{iac} + N'_{ic}\varepsilon''_{iab} + M''_{iab}\kappa'_{ic} + M''_{iac}\kappa'_{ib} + M''_{ibc}\kappa'_{ia}\Bigg)d\Omega\Bigg]u_au_bu_c
\end{aligned} \tag{55}$$

Lastly, using $\delta\boldsymbol{u} = \boldsymbol{u_d} = \{\cdots, u_d, \cdots\}^\intercal$, the fourth Fréchet derivative gives:

$$\begin{aligned}
\phi_c^{iv}\boldsymbol{u_a u_b u_c u_d} = &\left[\frac{1}{2}\int_\Omega \left(\cancelto{0}{N'''_{iabd}\varepsilon'_{ic}} + N''_{iab}\varepsilon''_{icd} + \cancelto{0}{N'''_{iacd}\varepsilon'_{ib}} + N''_{iac}\varepsilon''_{ibd} + N''_{iad}\varepsilon''_{ibc} + N'_{ia}\cancelto{0}{\varepsilon'''_{ibcd}} + \cancelto{0}{N'''_{ibcd}\varepsilon'_{ia}}\right.\right.\\
&+ N''_{ibc}\varepsilon''_{iad} + N''_{ibd}\varepsilon''_{iac} + N'_{ib}\cancelto{0}{\varepsilon'''_{iacd}} + N''_{icd}\varepsilon''_{iab} + N'_{ic}\cancelto{0}{\varepsilon'''_{iabd}} + \cancelto{0}{M'''_{iabd}\kappa'_{ic}} + M''_{iab}\cancelto{0}{\kappa''_{icd}} + \cancelto{0}{M'''_{iacd}\kappa'_{ib}}\\
&\left.\left. + M''_{iac}\cancelto{0}{\kappa''_{ibd}} + \cancelto{0}{M'''_{ibcd}\kappa'_{ia}} + M''_{ibc}\cancelto{0}{\kappa''_{iad}}\right)d\Omega\right]u_a u_b u_c u_d\\
= &\left[\frac{1}{2}\int_\Omega \left(N''_{iab}\varepsilon''_{icd} + N''_{iac}\varepsilon''_{ibd} + N''_{iad}\varepsilon''_{ibc} + N''_{ibc}\varepsilon''_{iad} + N''_{ibd}\varepsilon''_{iac} + N''_{icd}\varepsilon''_{iab}\right)d\Omega\right]u_a u_b u_c u_d
\end{aligned} \tag{56}$$

It is now possible to compute the functional differentiations corresponding to the second expansion of the total potential energy functional, about λ. From Eq. 54, the first differentiation about λ becomes:

$$\begin{aligned}
\dot{\phi}''_c\boldsymbol{u_a u_b} = &\left[\frac{1}{2}\int_\Omega \left(\cancelto{0}{\dot{N}'_{iab}\varepsilon_i} + N''_{iab}\dot{\varepsilon}_i + \dot{N}'_{ia}\varepsilon'_{ib} + N'_{ia}\dot{\varepsilon}'_{ib} + \dot{N}'_{ib}\varepsilon'_{ia} + N'_{ib}\dot{\varepsilon}'_{ia} + \dot{N}_i\varepsilon''_{iab}\right.\right.\\
&\left.\left. + N_i\cancelto{0}{\dot{\varepsilon}'''_{iab}} + \cancelto{0}{\dot{M}'_{iab}\kappa_i} + M''_{iab}\dot{\kappa}_i + \dot{M}'_{ia}\kappa'_{ib} + M'_{ia}\cancelto{0}{\dot{\kappa}''_{ib}} + \dot{M}'_{ib}\kappa'_{ia} + M'_{ib}\cancelto{0}{\dot{\kappa}''_{ia}}\right)d\Omega\right]u_a u_b\\
= &\left[\frac{1}{2}\int_\Omega \left(N''_{iab}\dot{\varepsilon}_i + \dot{N}'_{ia}\varepsilon'_{ib} + N'_{ia}\dot{\varepsilon}'_{ib} + \dot{N}'_{ib}\varepsilon'_{ia} + N'_{ib}\dot{\varepsilon}'_{ia} + \dot{N}_i\varepsilon''_{iab} + M''_{iab}\dot{\kappa}_i + \dot{M}'_{ia}\kappa'_{ib} + \dot{M}'_{ib}\kappa'_{ia}\right)d\Omega\right]u_a u_b
\end{aligned} \tag{57}$$

The second differentiation of ϕ''_c about λ becomes:

$$\begin{aligned}
\ddot{\phi}''_c\boldsymbol{u_a u_b} = &\left[\frac{1}{2}\int_\Omega \left(\cancelto{0}{\ddot{N}'_{iab}\varepsilon_i} + N''_{iab}\ddot{\varepsilon}_i + \cancelto{0}{\ddot{N}'_{ia}\varepsilon'_{ib}} + 2\dot{N}'_{ia}\dot{\varepsilon}'_{ib} + N'_{ia}\cancelto{0}{\ddot{\varepsilon}'_{ib}} + \cancelto{0}{\ddot{N}'_{ib}\varepsilon'_{ia}} + 2\dot{N}'_{ib}\dot{\varepsilon}'_{ia}\right.\right.\\
&\left.\left. + N'_{ib}\cancelto{0}{\ddot{\varepsilon}'_{ia}} + \ddot{N}_i\varepsilon''_{iab} + \dot{N}_i\cancelto{0}{\dot{\varepsilon}'''_{iab}} + \cancelto{0}{\dot{M}'_{iab}\dot{\kappa}_i} + M''_{iab}\ddot{\kappa}_i + \ddot{M}'_{ia}\kappa'_{ib} + \dot{M}'_{ia}\cancelto{0}{\dot{\kappa}''_{ib}} + \cancelto{0}{\ddot{M}'_{ib}\kappa'_{ia}} + \dot{M}'_{ib}\cancelto{0}{\dot{\kappa}''_{ia}}\right)d\Omega\right]u_a u_b\\
= &\left[\frac{1}{2}\int_\Omega \left(N''_{iab}\ddot{\varepsilon}_i + 2\dot{N}'_{ia}\dot{\varepsilon}'_{ib} + 2\dot{N}'_{ib}\dot{\varepsilon}'_{ia} + \ddot{N}_i\varepsilon''_{iab}\right)d\Omega\right]u_a u_b
\end{aligned} \tag{58}$$

The first differentiation of ϕ'''_c can be calculated based on Eq. 55 as:

$$\begin{aligned}
\dot{\phi}'''_c\boldsymbol{u_a u_b u_c} = &\left[\frac{1}{2}\int_\Omega \left(\cancelto{0}{\dot{N}'_{iab}\varepsilon'_{ic}} + N''_{iab}\dot{\varepsilon}'_{ic} + \cancelto{0}{\dot{N}'_{iac}\varepsilon'_{ib}} + N''_{iac}\dot{\varepsilon}'_{ib} + \dot{N}'_{ia}\varepsilon''_{ibc} + N'_{ia}\cancelto{0}{\dot{\varepsilon}''_{ibc}} + \cancelto{0}{\dot{N}'_{ibc}\varepsilon'_{ia}}\right.\right.\\
&+ N''_{ibc}\dot{\varepsilon}'_{ia} + \dot{N}'_{ib}\varepsilon''_{iac} + N'_{ib}\cancelto{0}{\dot{\varepsilon}''_{iac}} + \dot{N}'_{ic}\varepsilon''_{iab} + N'_{ic}\cancelto{0}{\dot{\varepsilon}''_{iab}} + \cancelto{0}{\dot{M}'_{iab}\kappa'_{ic}} + M''_{iab}\cancelto{0}{\dot{\kappa}''_{ic}} + \cancelto{0}{\dot{M}'_{iac}\kappa'_{ib}}\\
&\left.\left. + M''_{iac}\cancelto{0}{\dot{\kappa}''_{ib}} + \cancelto{0}{\dot{M}'_{ibc}\kappa'_{ia}} + M''_{ibc}\cancelto{0}{\dot{\kappa}''_{ia}}\right)d\Omega\right]u_a u_b u_c\\
= &\left[\frac{1}{2}\int_\Omega \left(N''_{iab}\dot{\varepsilon}'_{ic} + N''_{iac}\dot{\varepsilon}'_{ib} + \dot{N}'_{ia}\varepsilon''_{ibc} + N''_{ibc}\dot{\varepsilon}'_{ia} + \dot{N}'_{ib}\varepsilon''_{iac} + \dot{N}'_{ic}\varepsilon''_{iab}\right)d\Omega\right]u_a u_b u_c
\end{aligned} \tag{59}$$

The second differentiation of ϕ_c''' about λ can be calculated from Eq. 59:

$$\ddot{\phi}_c''' \boldsymbol{u_a u_b u_c} = \left[\frac{1}{2}\int_\Omega \left(\cancelto{0}{\dot{N}_{iab}''\dot{\varepsilon}_{ic}'} + N_{iab}''\cancelto{0}{\ddot{\varepsilon}_{ic}'} + \cancelto{0}{\dot{N}_{iac}''\dot{\varepsilon}_{ib}'} + N_{iac}''\cancelto{0}{\ddot{\varepsilon}_{ib}'} + \cancelto{0}{\ddot{N}_{ia}'\varepsilon_{ibc}''} + \dot{N}_{ia}'\cancelto{0}{\dot{\varepsilon}_{ibc}''} + \cancelto{0}{\dot{N}_{ibc}''\dot{\varepsilon}_{ia}'} + N_{ibc}''\cancelto{0}{\ddot{\varepsilon}_{ia}'} + \cancelto{0}{\ddot{N}_{ib}'\varepsilon_{iac}''} + \dot{N}_{ib}'\cancelto{0}{\dot{\varepsilon}_{iac}''} + \cancelto{0}{\ddot{N}_{ic}'\varepsilon_{iab}''} + \dot{N}_{ic}'\cancelto{0}{\dot{\varepsilon}_{iab}''}\right)d\Omega\right] u_a u_b u_c = 0 \tag{60}$$

The first and second differentiation of ϕ_c^{iv} with respect to λ can be calculated based on Eq. 56:

$$\dot{\phi}_c^{iv} \boldsymbol{u_a u_b u_c u_d} = \left[\frac{1}{2}\int_\Omega \left(\cancelto{0}{\dot{N}_{iab}''\varepsilon_{icd}''} + N_{iab}''\cancelto{0}{\dot{\varepsilon}_{icd}''} + \cancelto{0}{\dot{N}_{iac}''\varepsilon_{ibd}''} + N_{iac}''\cancelto{0}{\dot{\varepsilon}_{ibd}''} + \cancelto{0}{\dot{N}_{iad}''\varepsilon_{ibc}''} + N_{iad}''\cancelto{0}{\dot{\varepsilon}_{ibc}''} + \cancelto{0}{\dot{N}_{ibc}''\varepsilon_{iad}''} + N_{ibc}''\cancelto{0}{\dot{\varepsilon}_{iad}''} + \cancelto{0}{\dot{N}_{ibd}''\varepsilon_{iac}''} + N_{ibd}''\cancelto{0}{\dot{\varepsilon}_{iac}''} + \cancelto{0}{\dot{N}_{icd}''\varepsilon_{iab}''} + N_{icd}''\cancelto{0}{\dot{\varepsilon}_{iab}''}\right)d\Omega\right] u_a u_b u_c u_d = 0 \tag{61}$$

$$\ddot{\phi}_c^{iv} \boldsymbol{u_a u_b u_c u_d} = 0 \tag{62}$$

V. Results

All the results herein presented were generated using the scripts provided in a publicly available data set [45]. The data set also includes the implementation of the SC-BFSC element previously presented.

A. Verification

Water's composite cylindrical shell is used as the first verification case. This shell has been investigated by Arbocz and Starnes [46], and used as a verification case by Rahman [44]. Water's shell is made of an 8-ply [±45/0/90]s laminate and its geometry and laminate data is shown in Table 1. The ply angles are measured with respect to the x axis, rotating about the z axis, with the axes defined according to Figure 1. **Boundary conditions:** the cylindrical shell is axially loaded and both ends have the classical simply supported boundary condition SS-3 [46], whereby the out-of-plane and circumferential displacements are fixed, whereas the axial displacements are kept free. The axial displacement is fixed at only one node located at the middle cross section of the cylinder. All rotations are kept free.

Table 1 Geometric and material properties of the composite cylindrical shell investigated by Water [46]

Lay-up	Total thickness [mm]	Cylinder length [mm]	Cylinder radius [mm]
$[\pm 45/0/90]_{sym}$	1.01539	335.6	203.18603

E_{11} $[GPa]$	E_{22} $[GPa]$	G_{12} $[GPa]$	ν_{12}
127.629	11.3074	6.00257	0.300235

B. Convergence analysis of the SC-BFSC

A convergence analysis is performed using element aspect ratios of $\ell y/\ell x = 1, 2, 3$, according to Figure 1. Tables 2 and 3 respectively show the results for Von Kármán and Sanders nonlinear kinematics. The number of nodes along the circumferential direction n_y is changed from 40 to 240, and the number of nodes along the axial direction n_x is calculated with $n_x = n_y L/(2\pi R(\ell y/\ell x))$. The mesh generator guarantees $n_x \mod 2 = 1$ to always create a row of nodes in the

Table 2 Convergence of critical linear buckling load for Water's cylinder using SC-BFSC with Von Kármán kinematics

	Aspect ratio $\ell y/\ell x = 1$			Aspect ratio $\ell y/\ell x = 2$			Aspect ratio $\ell y/\ell x = 3$		
n_y	n_x	DOF	Load	n_x	DOF	Load	n_x	DOF	Load
40	11	4400	127.32745	23	9200	123.39947	33	13200	122.70039
60	17	10200	143.71740	33	19800	142.92665	51	30600	142.68585
80	23	18400	143.66714	**45**	**36000**	143.29293	67	53600	143.20413
100	27	27000	143.52886	55	55000	143.27813	83	83000	143.22877
120	33	39600	143.38488	67	80400	143.23133	101	121200	143.20075
140	39	54600	143.30871	77	107800	143.20703	117	163800	143.18490
160	45	72000	143.26379	89	142400	143.19030	133	212800	143.17476
180	51	91800	143.23497	101	181800	143.17930	151	271800	143.16756
200	55	110000	143.21967	111	222000	143.17221	167	334000	143.16266
220	61	134200	143.20441	123	270600	143.16649	183	402600	143.15900
240	67	160800	143.19321	133	319200	143.16252	201	482400	143.15608

middle cross section. An asymptotic convergence is observed, and the mesh $n_y = 80$ and $n_x = 45$ is selected for all the studies presented in this manuscript, corresponding to a model with 3600 nodes and 36000 degrees-of-freedom.

Using a linear pre-buckling state, the convergence of $b_{1-1-1-1}$ obtained with Sanders kinematics is presented in Table 4. To compare with the implementation available in DIANA [47], it is assumed that for a linear pre-buckling state, ϕ_c'' of Eq. 54 is calculated with $\phi_c'' = \boldsymbol{K} + \lambda_{cr}\boldsymbol{K_{G0}}$, where λcr is the first linear buckling eigenvalue, $\boldsymbol{K}$ is the linear constitutive stiffness matrix and $\boldsymbol{K_{G0}}$ the geometric stiffness matrix as defined per Eq. 26. Furthermore, all nonlinear terms are ignored in the calculation of $\dot{\boldsymbol{\varepsilon}}$, as per Eq. 36 in the case of Von Kármán kinematics, or Eq. 41 for Sanders-type kinematics. Additionally, all nonlinear terms are ignored in the calculation of $\boldsymbol{\varepsilon}_a'$, as given in Eq. 34 for Von Kármán kinematics, and in Eq. 39 for Sanders kinematics. A good convergence of $b_{1-1-1-1}$ is also observed with the mesh $n_y = 80$ and $n_x = 45$, corresponding to a model with 3600 nodes and 36000 degrees-of-freedom.

C. Linear buckling analysis

The first 24 linear buckling modes of Water's composite cylindrical obtained with the SC-BFSC element, using the selected mesh size, are compared against DIANA CQ40L element. The results presented in Table 5 show that the SC-BFSC element with Sanders kinematics is able to approach the reference results closer than with Von Kármán kinematics, as expected. The attempt to force classical plate kinematics in Abaqus by using transverse stiffnesses of $1000 \times G_{13}$ and $1000 \times G_{23}$ produced results that are closer to the SC-BFSC with Von Kármán and Sanders kinematics, both based on classic shell kinematics. Figure 3 shows that the first linear buckling mode for Water's shell has 14 half-waves. The simplified shell kinematics obtained with Von Kármán nonlinear equations is not able to describe the first linear buckling mode shapes, as shown by Figure 4-a. On the other hand, Sanders kinematics are able to also capure 14 half-waves for the first linear buckling mode, as shown in Figure 4-b.

D. Perturbation analysis

A perturbation analysis with linear pre-buckling state is performed and the results for the diagonal terms $b_{i-i-i-i}$, for $i = 1, 2, \cdots, 10$ are presented on Table 6. There is a close match with DIANA CQ40L elements up to mode 8, and it was observed that modes 9 and 10 from the SC-BFSC mesh correspond to modes 11 and 12 from DIANA CQ40L mesh. This mode switch is expected, especially observing in Table 5 the small proximity of the linear buckling eigenvalues.

In order to evaluate the off-diagonal terms for the $b_{i-j-k-\ell}$ factors, a perturbation analysis considering the interaction between modes 1, 3, and 5 of Table 5 is performed. Again, a linear pre-buckling state is assumed. The results presented in Table 7 show a close agreement between the SC-BFSC element using Sanders kinematics and DIANA CQ40L element.

Table 3 Convergence of critical linear buckling load for Water's cylinder using SC-BFSC with Sanders-type kinematics

	Aspect ratio $\ell y/\ell x = 1$			Aspect ratio $\ell y/\ell x = 2$			Aspect ratio $\ell y/\ell x = 3$		
n_y	n_x	DOF	Load	n_x	DOF	Load	n_x	DOF	Load
40	11	4400	126.95431	23	9200	123.08702	33	13200	122.39329
60	17	10200	140.83009	33	19800	140.22962	51	30600	140.10289
80	23	18400	140.78053	**45**	**36000**	140.49394	67	53600	140.43742
100	27	27000	140.70037	55	55000	140.49747	83	83000	140.46084
120	33	39600	140.60686	67	80400	140.47566	101	121200	140.45166
140	39	54600	140.54983	77	107800	140.45943	117	163800	140.44140
160	45	72000	140.51293	89	142400	140.44582	133	212800	140.43284
180	51	91800	140.48780	101	181800	140.43597	151	271800	140.42598
200	55	110000	140.47408	111	222000	140.42922	167	334000	140.42093
220	61	134200	140.45986	123	270600	140.42360	183	402600	140.41701
240	67	160800	140.44921	133	319200	140.41959	201	482400	140.41383

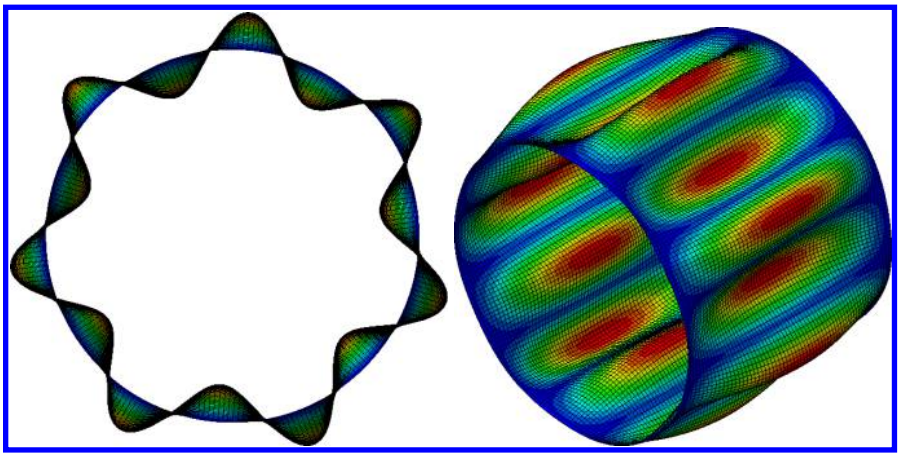

Fig. 3 Water's cylinder first linear buckling mode, obtained with Abaqus.

VI. Concluding remarks and future research

The displacement-based formulation for the multi-modal Koiter approach was successfully extended from the work of Castro and Jansen [13] and applied for the case of cylindrical shells. A verification using the commercial finite element software DIANA [47] was performed, showing that only Sanders nonlinear kinematics was able to accurately capture the first linear buckling shape of Water's cylindrical shell. Therefore, the authors recommend Sanders kinematics for future analyses using the methodology herein presented. The implemented algorithms are based on state-of-the-art open source packages and are made publicly available in a data set [45].

The present methodology is applicable for the case a nonlinear pre-buckling state, or fundamental state. Future studies will focus on the formulation and nonlinear algorithm for the nonlinear fundamental state. Moreover, the influence of the pre-buckling load level on the calculated $b_{i-j-k-\ell}$ coefficients will be investigated, with the aim to achieve a fast method to accurately predict the post-buckling behavior of imperfection-sensitive shells.

Future research will focus on the direct application of the methodology herein proposed, implemented as provided in the publicly available data set [45]. The investigation will aim at finding imperfection-insensitive shell designs [48, 49]. The authors will develop design parameterization schemes enabled by novel manufacturing techniques, such as automated fibre placement [50, 51], continuous tow shearing [52], and variable-angle filament winding [27, 53, 54]. These novel designs should focus on nonlinear stiffness constraints constraints and explore the effect of overlaps that are created by the nonlinear coupling between the steering angle and the laminate thickness, as already investigated by

Table 4 Convergence of $b_{1-1-1-1}$ using linear pre-buckling state for Water's cylinder using SC-BFSC with Sanders-type kinematics

	Aspect ratio $\ell y/\ell x = 1$			Aspect ratio $\ell y/\ell x = 2$			Aspect ratio $\ell y/\ell x = 3$		
n_y	n_x	DOF	$b_{1-1-1-1}$	n_x	DOF	$b_{1-1-1-1}$	n_x	DOF	$b_{1-1-1-1}$
40	11	4400	-0.00850561	23	9200	-0.23054820	33	13200	-0.25462784
50	13	6500	-0.04331440	27	13500	-0.04445266	41	20500	-0.18060378
60	17	10200	-0.04501454	33	19800	-0.04539179	51	30600	-0.04536920
70	19	13300	-0.04595095	39	27300	-0.04854888	59	41300	-0.04664120
80	23	18400	-0.04574508	**45**	**36000**	-0.04589748	67	53600	-0.04592220
90	25	22500	-0.04587003	51	45900	-0.04599877	75	67500	-0.04598445
100	27	27000	-0.04596100	55	55000	-0.04602548	83	83000	-0.04603055
120	33	39600	-0.04603133	67	80400	-0.04607434	101	121200	-0.04608576
140	39	54600	-0.04643624	77	107800	-0.04642807	117	163800	-0.04687716
160	45	72000	-0.04609398	89	142400	-0.04610874	133	212800	-0.04609925
180	51	91800	-0.04609431	101	181800	-0.04610630	151	271800	-0.04609760
200	55	110000	-0.04609543	111	222000	-0.04610086	167	334000	-0.04609990
220	61	134200	-0.04610482	123	270600	-0.04610675	183	402600	-0.04610172
240	67	160800	-0.04610227	133	319200	-0.04610134	201	482400	-0.04610653

Castro and collaborators [55, 56] in the design of plates, Machado et al. in the design of wing panels [57], Lincoln et al. in the design of cylindrical shells [49].

CRediT authorship contribution statement

S.G.P. Castro: Conceptualization, methodology, formal analysis, investigation, validation, software, data curation, writing - original draft preparation, writing - editing. **E. L. Jansen**: Validation, formal analysis.

References

[1] Koiter, W. T., "The Stability of Elastic Equilibrium," Ph.D. thesis, Translation by Eduard Riks, Technical Report AFFDL-TR-70-25, February 1970. Delft University of Technology, 1945.

[2] Cohen, G. A., "Effect of a nonlinear prebuckling state on the postbuckling behavior and imperfect on sensitivity of elastic structures." *AIAA Journal*, Vol. 6, No. 8, 1968, pp. 1616–1619. https://doi.org/10.2514/3.4832.

[3] Arbocz, J., and Hol, J., "Koiter's stability theory in a computeraided engineering (CAE) environment," *International Journal of Solids and Structures*, Vol. 26, No. 9-10, 1990, pp. 945–973. https://doi.org/10.1016/0020-7683(90)90011-J.

[4] Olesen, J. F., and Byskov, E., "Accurate determination of asymptotic postbuckling stresses by the finite element method," *Computers & Structures*, Vol. 15, No. 2, 1982, pp. 157–163. https://doi.org/10.1016/0045-7949(82)90063-3.

[5] Peek, R., and Kheyrkhahan, M., "Postbuckling behavior and imperfection sensitivity of elastic structures by the Lyapunov-Schmidt-Koiter approach," *Computer Methods in Applied Mechanics and Engineering*, Vol. 108, No. 3-4, 1993, pp. 261–279. https://doi.org/10.1016/0045-7825(93)90005-I.

[6] Menken, C., Schreppers, G., Groot, W., and Petterson, R., "Analyzing buckling mode interactions in elastic structures using an asymptotic approach; theory and experiments," *Computers & Structures*, Vol. 64, No. 1-4, 1997, pp. 473–480. https://doi.org/10.1016/S0045-7949(96)00139-3.

[7] Casciaro, R., Garcea, G., Attanasio, G., and Giordano, F., "Perturbation approach to elastic post-buckling analysis," *Computers & Structures*, Vol. 66, No. 5, 1998, pp. 585–595. https://doi.org/10.1016/S0045-7949(97)00112-0.

Table 5 Verification of linear buckling results for Water's composite cylindrical shell

Eigenvalue	DIANA CQ40L	Abaqus FSDT	Abaqus CLT*	SC-BFSC Donnell	SC-BFSC Sanders
1	136.92	136.948	137.391	143.29293	140.49394
2	136.92	136.948	137.391	143.29293	140.49394
3	140.58	140.591	145.741	143.35628	142.43000
4	140.58	140.591	145.741	143.35628	142.43000
5	140.90	140.898	145.749	143.40197	142.64724
6	140.90	140.898	145.749	143.40197	142.64724
7	141.33	141.343	145.870	144.52421	143.38945
8	141.33	141.343	145.870	144.52421	143.38945
9	142.41	142.416	145.971	144.90640	144.32033
10	142.41	142.416	145.971	144.90640	144.32033
11	142.60	142.587	146.023	145.88033	144.77923
12	142.60	142.587	146.023	145.88033	144.77923
13	144.48	144.473	146.113	145.91021	145.85476
14	144.48	144.473	146.113	145.91021	145.85476
15	144.48	144.476	146.411	146.00440	145.85662
16	144.48	144.476	146.411	146.00440	145.85662
17	144.71	144.692	146.456	146.12549	146.07182
18	144.71	144.692	146.456	146.12549	146.07182
19	144.75	144.744	146.557	146.14758	146.13286
20	144.75	144.744	146.557	146.14758	146.13286
21	145.19	145.168	147.048	146.67647	146.58686
22	145.19	145.168	147.048	146.67647	146.58686
23	145.27	145.264	147.116	146.74180	146.66934
24	145.27	145.264	147.116	146.74180	146.66934

*Attempted CLT kinematics by using $1000 \times G_{13}, 1000 \times G_{23}$ in the shell models.

[8] Kheyrkhahan, M., and Peek, R., "Postbuckling analysis and imperfection sensitivity of general shells by the finite element method," *International Journal of Solids and Structures*, Vol. 36, No. 18, 1999, pp. 2641–2681. https://doi.org/10.1016/S0020-7683(98)00129-2.

[9] Casciaro, R., "Computational asymptotic post-buckling analysis of slender elastic structures," *Phenomenological and Mathematical Modelling of Structural Instabilities*, Vol. 470, Springer Vienna, Vienna, 2005, pp. 195–276. https://doi.org/10.1007/3-211-38028-0_4.

[10] Rahman, T., Ijsselmuiden, S. T., Abdalla, M. M., and Jansen, E. L., "Postbuckling analysis of variable stiffness composite plates using a finite element-based perturbation method," *International Journal of Structural Stability and Dynamics*, Vol. 11, No. 04, 2011, pp. 735–753. https://doi.org/10.1142/S0219455411004324.

[11] Henrichsen, S. R., Weaver, P. M., Lindgaard, E., and Lund, E., "Post-buckling optimization of composite structures using Koiter's method," *International Journal for Numerical Methods in Engineering*, Vol. 108, No. 8, 2016, pp. 902–940. https://doi.org/10.1002/nme.5239.

[12] Madeo, A., Groh, R. M., Zucco, G., Weaver, P. M., Zagari, G., and Zinno, R., "Post-buckling analysis of variable-angle tow composite plates using Koiter's approach and the finite element method," *Thin-Walled Structures*, Vol. 110, 2017, pp. 1–13. https://doi.org/10.1016/j.tws.2016.10.012.

[13] Castro, S., and Jansen, E., "Displacement-based formulation of Koiter's method: Application to multi-modal post-buckling finite element analysis of plates," *Thin-Walled Structures*, Vol. 159, 2021, p. 107217. https://doi.org/10.1016/j.tws.2020.107217.

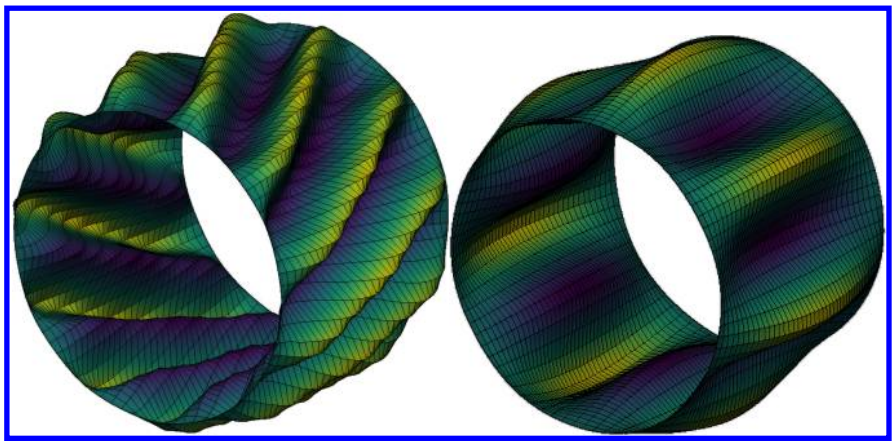

(a) Von Kármán kinematics (b) Sanders kinematics

Fig. 4 Water's cylinder first linear buckling mode, obtained with the SC-BFSC element.

Table 6 Water's cylinder results for $b_{i-i-i-i}$ with $i = 1, 2, \cdots, 10$.

$b_{i-i-i-i}$	DIANA CQ40L	SC-BFSC Sanders
$b_{1-1-1-1}$	-0.044816	-0.04589677
$b_{2-2-2-2}$	-0.044812	-0.04589691
$b_{3-3-3-3}$	0.152130	0.15117576
$b_{4-4-4-4}$	0.152250	0.15123392
$b_{5-5-5-5}$	0.231540	0.23508782
$b_{6-6-6-6}$	0.231570	0.23522304
$b_{7-7-7-7}$	0.056992	0.05563493
$b_{8-8-8-8}$	0.056953	0.05561389
$b_{9-9-9-9}$	-0.086166	0.29929214
$b_{10-10-10-10}$	-0.086093	0.29919679

[14] Rahman, T., and Jansen, E. L., "Finite element based coupled mode initial post-buckling analysis of a composite cylindrical shell," *Thin-Walled Structures*, Vol. 48, No. 1, 2010, pp. 25–32. https://doi.org/10.1016/j.tws.2009.08.003.

[15] Barbero, E. J., Madeo, A., Zagari, G., Zinno, R., and Zucco, G., "Imperfection sensitivity analysis of composite cylindrical shells using Koiter's method," *International Journal for Computational Methods in Engineering Science and Mechanics*, Vol. 18, No. 1, 2017, pp. 105–111. https://doi.org/10.1080/15502287.2016.1276359.

[16] Jansen, E., Rahman, T., and Rolfes, R., "Finite Element Integrated Fast Buckling Analysis Tools Using a Perturbation Approach," *Buckling and Postbuckling Structures II: Experimental, Analytical and Numerical Studies*, World Scientific Publishing Co. Pte. Ltd., 2018, pp. 147–171. https://doi.org/10.1142/9781786344335_0005.

[17] Sun, Y., Tian, K., Li, R., and Wang, B., "Accelerated Koiter method for post-buckling analysis of thin-walled shells under axial compression," *Thin-Walled Structures*, Vol. 155, 2020, p. 106962. https://doi.org/10.1016/j.tws.2020.106962.

[18] Groh, R. M., and Pirrera, A., "Spatial chaos as a governing factor for imperfection sensitivity in shell buckling," *Physical Review E*, Vol. 100, No. 3, 2019. https://doi.org/10.1103/PhysRevE.100.032205.

[19] Xia, J., Farrell, P. E., and Castro, S. G., "Nonlinear bifurcation analysis of stiffener profiles via deflation techniques," *Thin-Walled Structures*, Vol. 149, 2020, p. 106662. https://doi.org/10.1016/j.tws.2020.106662.

[20] Budiansky, B., "Theory of Buckling and Post-Buckling Behavior of Elastic Structures," *Advances in Applied Mechanics*, Vol. 14, 1974, pp. 1–65. https://doi.org/10.1016/S0065-2156(08)70030-9.

Table 7 Water's cylinder results for $b_{i-j-k-\ell}$ coefficients for buckling modes modes 1, 3 and 5.

$b_{i-j-k-\ell}$	DIANA CQ40L	SC-BFSC Sanders
$b_{1-1-1-1}$	−0.044816	−0.045897
$b_{1-1-3-3}$	−0.162320	−0.156857
$b_{1-1-5-5}$	−0.258970	−0.257206
$b_{1-3-1-3}$	−0.294970	−0.315608
$b_{1-3-3-1}$	−0.162320	−0.156857
$b_{1-5-1-5}$	−0.473790	−0.516461
$b_{1-5-5-1}$	−0.258970	−0.257206
$b_{3-1-1-3}$	−0.014080	−0.013432
$b_{3-1-3-1}$	−0.025586	−0.027027
$b_{3-3-1-1}$	−0.014080	−0.013432
$b_{3-3-3-3}$	0.152130	0.151176
$b_{3-3-5-5}$	0.104770	0.106281
$b_{3-5-3-5}$	−0.030061	−0.031597
$b_{3-5-5-3}$	0.104770	0.106281
$b_{5-1-1-5}$	−0.015632	−0.015043
$b_{5-1-5-1}$	−0.028599	−0.030206
$b_{5-3-3-5}$	0.072907	0.072587
$b_{5-3-5-3}$	−0.020919	−0.021580
$b_{5-5-1-1}$	−0.015632	−0.015043
$b_{5-5-3-3}$	0.072907	0.072587
$b_{5-5-5-5}$	0.231540	0.235088

[21] Castro, S. G., Zimmermann, R., Arbelo, M. A., Khakimova, R., Hilburger, M. W., and Degenhardt, R., "Geometric imperfections and lower-bound methods used to calculate knock-down factors for axially compressed composite cylindrical shells," *Thin-Walled Structures*, Vol. 74, 2014, pp. 118–132. https://doi.org/10.1016/j.tws.2013.08.011.

[22] Franzoni, F., Odermann, F., Lanbans, E., Bisagni, C., Andrés Arbelo, M., and Degenhardt, R., "Experimental validation of the vibration correlation technique robustness to predict buckling of unstiffened composite cylindrical shells," *Composite Structures*, Vol. 224, 2019, p. 111107. https://doi.org/10.1016/j.compstruct.2019.111107.

[23] Labans, E., Abramovich, H., and Bisagni, C., "An experimental vibration-buckling investigation on classical and variable angle tow composite shells under axial compression," *Journal of Sound and Vibration*, Vol. 449, 2019, pp. 315–329. https://doi.org/10.1016/j.jsv.2019.02.034.

[24] Rahman, T., and Jansen, E., "Finite element based coupled mode initial post-buckling analysis of a composite cylindrical shell," *Thin-Walled Structures*, Vol. 48, No. 1, 2010, pp. 25–32. https://doi.org/10.1016/j.tws.2009.08.003.

[25] Arfken, G. B., Weber, H. J., and Spector, D., "Mathematical Methods for Physicists, 4th ed ." *American Journal of Physics*, Vol. 67, No. 2, 1999, pp. 165–169. https://doi.org/10.1119/1.19217.

[26] Bogner, F. K., Fox, R. L., and Schmit Jr., L. A., "The generation of inter-element-compatible stiffness and mass matrices by the use of interpolation formulas," *Matrix Methods in Structural Mechanics*, AirForce Inst. of Tech., Wright Patterson AF Base, Cleveland, Ohio, 1966, pp. 395–444. URL http://contrails.iit.edu/reports/8569.

[27] Wang, Z., Almeida Jr, J. H. S., Ashok, A., Wang, Z., and Castro, S. G. P., "Lightweight design of variable-angle filament-wound cylinders combining Kriging-based metamodels with particle swarm optimization," *Preprint*, 2021. https://doi.org/10.31224/osf.io/3ym95.

[28] Ochoa, O. O., and Reddy, J. N., "Finite Element Analysis of Composite Laminates," *Finite Element Analysis of Composite Laminates*, Springer, Dordrecht, 1992, pp. 37–109. https://doi.org/10.1007/978-94-015-7995-7_3.

[29] Tsunematsu, D. Q., "The aeroelastic behavior of laminated composite panels undergoing progressive damage in supersonic flow," Thesis of doctor of science, Instituto Tecnológico de Aeronáutica, 2019.

[30] Tsunematsu, D. Q., and Donadon, M. V., "Aeroelastic behavior of composite panels undergoing progressive damage," *Composite Structures*, Vol. 210, 2019, pp. 458–472. https://doi.org/10.1016/J.COMPSTRUCT.2018.11.065.

[31] Barbero, E. J., Reddy, J. N., and Teply, J. L., "General two-dimensional theory of laminated cylindrical shells," *AIAA Journal*, Vol. 28, No. 3, 1990, pp. 544–553. https://doi.org/10.2514/3.10426.

[32] Reddy, J. N., *Mechanics of Laminated Composite Plates and Shells*, 2nd ed., CRC Press, 2003. https://doi.org/10.1201/b12409.

[33] Donnell, L., "Stability of Thin-walled Tubes under Torsion," Tech. Rep. 479, NACA Report No. 479, 1933.

[34] Donnell, L. H., "A new theory for the buckling of thin cylinders under axial compression and bending," *Trans. ASME*, Vol. 56, No. 11, 1934, pp. 795–806.

[35] Sanders, J. L., "Nonlinear theories for thin shells," *Quarterly of Applied Mathematics*, Vol. 21, No. 1, 1963, pp. 21–36. URL http://www.jstor.org/stable/43634948.

[36] Simitses, G., Sheinman, I., and Shaw, D., "The accuracy of Donnell's equations for axially-loaded, imperfect orthotropic cylinders," *Computers & Structures*, Vol. 20, No. 6, 1985, pp. 939–945. https://doi.org/10.1016/0045-7949(85)90013-6.

[37] Silvestre, N., Wang, C., Zhang, Y., and Xiang, Y., "Sanders shell model for buckling of single-walled carbon nanotubes with small aspect ratio," *Composite Structures*, Vol. 93, No. 7, 2011, pp. 1683–1691. https://doi.org/10.1016/j.compstruct.2011.01.004.

[38] Goldfeld, Y., Sheinman, I., and Baruch, M., "Imperfection Sensitivity of Conical Shells," *AIAA Journal*, Vol. 41, No. 3, 2003, pp. 517–524. https://doi.org/10.2514/2.1976.

[39] Goldfeld, Y., "Imperfection sensitivity of laminated conical shells," *International Journal of Solids and Structures*, Vol. 44, No. 3-4, 2007, pp. 1221–1241. https://doi.org/10.1016/j.ijsolstr.2006.06.016.

[40] Castro, S. G. P., "Semi-Analytical Tools for the Analysis of Laminated Composite Cylindrical and Conical Imperfect Shells under Various Loading and Boundary Conditions," Ph.D. thesis, Technische Universität Clausthal, 2014.

[41] Castro, S., Mittelstedt, C., Monteiro, F., Arbelo, M., Ziegmann, G., and Degenhardt, R., "Linear buckling predictions of unstiffened laminated composite cylinders and cones under various loading and boundary conditions using semi-analytical models," *Composite Structures*, Vol. 118, 2014, pp. 303–315. https://doi.org/10.1016/j.compstruct.2014.07.037.

[42] Knyazev, A. V., "Toward the Optimal Preconditioned Eigensolver: Locally Optimal Block Preconditioned Conjugate Gradient Method," *SIAM Journal on Scientific Computing*, Vol. 23, No. 2, 2001, pp. 517–541. https://doi.org/10.1137/S1064827500366124.

[43] Virtanen, P., Gommers, R., Oliphant, T. E., and et al., "SciPy 1.0: Fundamental Algorithms for Scientific Computing in Python," *Nature Methods*, Vol. 17, 2020, pp. 261–272. https://doi.org/10.1038/s41592-019-0686-2.

[44] Rahman, T., "A perturbation approach for geometrically nonlinear structural analysis using a general purpose finite element code," Ph.D. thesis, Delft University of Technology, 2009. URL http://resolver.tudelft.nl/uuid:80e11dbd-90be-44f1-bb36-049503a265bd.

[45] Castro, S. G. P., "Data set for Displacement-based multi-modal formulation of Koiter's method applied to cylindrical shells. (Version 2021-12-03) [Data set]." , Dec. 2021. https://doi.org/10.5281/zenodo.5667978.

[46] Arbocz, J., and Starnes, J. H., "On a High-Fidelity Hierarchical Approach to Buckling Load Calculations," *New Approaches to Structural Mechanics, Shells and Biological Structures*, SpringerLink, 2002, pp. 271–292. https://doi.org/10.1007/978-94-015-9930-6_22.

[47] Manie, J., "DIANA 10.2 User's Manual," , 2017.

[48] White, S. C., and Weaver, P. M., "Towards imperfection insensitive buckling response of shell structures-shells with plate-like post-buckled responses," *The Aeronautical Journal*, Vol. 120, No. 1224, 2016, p. 233–253. https://doi.org/10.1017/aer.2015.14.

[49] Lincoln, R., Weaver, P., Pirrera, A., and Groh, R., "Imperfection-insensitive continuous tow-sheared cylinders," *Composite Structures*, Vol. 260, 2021, p. 113445. https://doi.org/10.1016/j.compstruct.2020.113445.

[50] Blom, A. W., Stickler, P. B., and Gürdal, Z., "Design and Manufacture of a Variable-Stiffness Cylindrical Shell," Tech. rep., 2009. URL https://repository.tudelft.nl/islandora/object/uuid%3A0d8a5de7-966a-4f80-bc5c-bc6bb1733410.

[51] Blom, A. W., Abdalla, M. M., and Gürdal, Z., "Optimization of course locations in fiber-placed panels for general fiber angle distributions," *Composites Science and Technology*, Vol. 70, No. 4, 2010, pp. 564–570. https://doi.org/10.1016/j.compscitech.2009.12.003.

[52] Kim, B. C., Potter, K., and Weaver, P. M., "Continuous tow shearing for manufacturing variable angle tow composites," *Composites Part A: Applied Science and Manufacturing*, Vol. 43, No. 8, 2012, pp. 1347–1356. https://doi.org/10.1016/j.compositesa.2012.02.024.

[53] Wang, Z., Almeida Jr., J. H. S., St-Pierre, L., Wang, Z., and Castro, S., "Reliability-based buckling optimization with an accelerated Kriging metamodel for filament-wound variable angle tow composite cylinders," *Composite Structures*, Vol. 254, 2020.

[54] Almeida, J. H. S., St-Pierre, L., Wang, Z., Ribeiro, M. L., Tita, V., Amico, S. C., and Castro, S. G., "Design, modeling, optimization, manufacturing and testing of variable-angle filament-wound cylinders," *Composites Part B: Engineering*, Vol. 225, 2021, p. 109224. https://doi.org/10.1016/j.compositesb.2021.109224.

[55] Vertonghen, L., and Castro, S. G., "Modelling of fibre steered plates with coupled thickness variation from overlapping continuous tows," *Composite Structures*, 2021, p. 113933. https://doi.org/10.1016/j.compstruct.2021.113933.

[56] Ummels, R., and Castro, S. G., "Overlap-stiffened panels for optimized buckling performance under minimum steering radius constraints," *Composites Part C: Open Access*, Vol. 6, 2021, p. 100174. https://doi.org/10.1016/j.jcomc.2021.100174.

[57] Machado, T. G., Hernandes, J. A., Capacia, V., and Castro, S. G., "Design of Compressed Variable Stiffness Panels with Steering-thickness Coupling," *AIAA Scitech 2021 Forum*, American Institute of Aeronautics and Astronautics, Reston, Virginia, 2021. https://doi.org/10.2514/6.2021-0568.